Chapter 6

LONGITUDINAL MICROWAVE INSTABILITY FOR PROTONS

6.1 Keil-Schnell Criterion

According to Eq. (2.10), a beam particle changes its energy per turn according to

$$\frac{d\Delta E}{dn} = eV_{\rm rf}[\sin(\phi_s - h\omega_0\tau) - \sin\phi_s] - [U(\delta) - U_s] + C_0(\langle F_0^{\parallel}\rangle - \langle F_{0s}^{\parallel}\rangle) \ , \qquad (6.1)$$

where the first two terms on the right represent, respectively, the rf focusing and radiation damping. The last term comes from the longitudinal wake potential [Eq. (2.7)]:

$$\langle F_0^{\parallel}(\tau)\rangle - \langle F_{0s}^{\parallel}\rangle = -\frac{e^2}{C_0}\left[\int_{-infty}^{\infty} d\tau'\rho(\tau')W_0'(\tau'-\tau) - \int_{-infty}^{\infty} d\tau'\rho(\tau')W_0'(\tau')\right] \ , \quad (6.2)$$

where $\rho(\tau)$ is the linear particle density of the beam for a particle that arrives τ earlier than the synchronous particle. For a purely inductive wake potential $W_0'(\tau) = L\delta'(\tau)$ $(\tau \geq 0)$ with L being the inductance, the energy gained per turn becomes

$$\frac{d\Delta E}{dn} = e^2 L\rho'(\tau) + \cdots \ , \qquad (6.3)$$

where we have only displayed the contribution of the wake potential and assumed $\rho'(0) = 0$.. Now consider a coasting beam with a very small momentum spread. If a small bump is developed along the beam and the vacuum chamber is inductive ($L > 0$), particles

at the front of the bump lose energy because $\rho'(\tau) < 0$, and particles at the rear of the bump gain energy because $\rho'(\tau) < 0$. Above transition ($\eta > 0$), particles at the front arrive earlier and particles at the rear arrive later. Thus the bump will be smoothed out, as illustrated in the left drawing in Fig. 6.1. The result will be the same if the beam sees a capacitive wake ($L < 0$) and is below transition. However, for capacitive wake above transition, particles at the front of the bump gain energy and will arrive later while those at the rear of the bump lose energy and will arrive earlier, thus enhancing the bump. The situation is the same for an inductive wake below transition. In other word, the situation is unstable against small nonuniformity in the linear distribution.

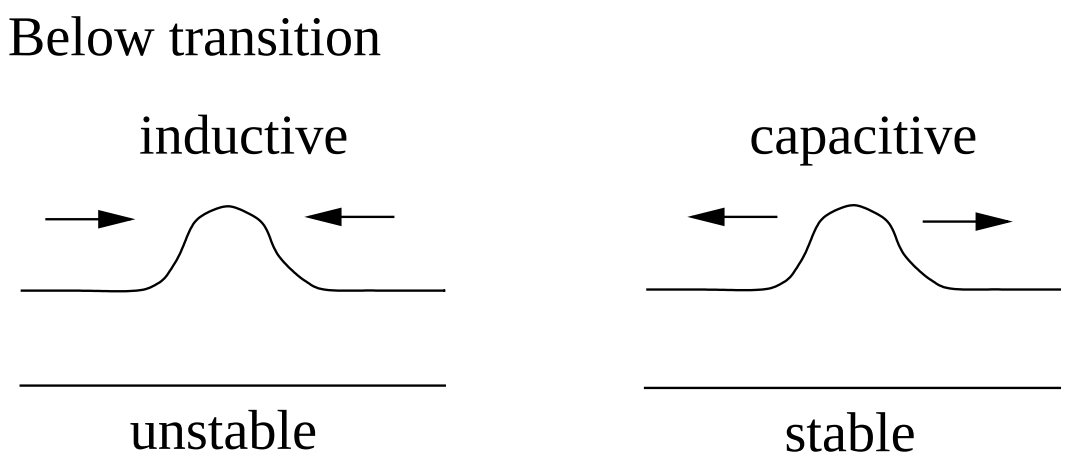

Figure 6.1: Below transition, a bump will be smoothed out under a capacitive force (right) and the beam will be stable against bump formation. However under an inductive force, the bump will continue to grow (left) and the beam will be unstable against small perturbations. Above transition, the opposite is true.

So far the momentum spread of particles in the beam has not been considered. In order for the bump to grow, the growth rate must be faster than phase-drifting rate coming from the momentum spread of the beam particles, otherwise the bump will be smeared. This damping process is called *Landau damping* [1]. The impedance driving the instability need not be purely reactive. It can be the real part of the impedance. Especially for a sharp bump, the driving frequency will be very high.

This same consideration can also be applied to a bunch provided that the growth must be faster than synchrotron frequency otherwise the bump will be smeared out. Needless to say, the size of the bump is much less than the length of the bunch. The driving impedance must therefore have a wavelength less than the length of the bunch.

This growth at high frequencies is called *microwave instability*. This discussion is very similar to that in Sec. 3.2. There, the concern is about the enhancement or partial cancellation of the rf focusing force at rf frequency; therefore an inductive force below transition or a capacitive force above transition is preferred to prevent bunch lengthening. Here, the concern is the evolution of a small bump at high frequencies. In order that a small bump will not grow, the opposite conclusion is obtained. In other words, to smooth out a bump. a capacitive force below transition or an inductive force above transition is preferred.

Because of the random quantum excitation in an electron bunch, there is a finite probability of having electrons jumping outside the bucket and getting lost. To increase the *quantum lifetime* of an electron bunch, a large rf bucket is necessary. Touschek scattering will also convert transverse momentum spread of electrons into longitudinal. In order that those electrons will not be lost, the rf bucket has to be large. For this reason, the bucket in an electron machine is in general very much larger than the size of the electron bunch, usually the height of the bucket is more than 10 times the rms energy spread of the bunch, in contrast with only about 3 times or less in proton machines. To achieve this, the rf voltage $V_{\rm rf}$ for an electron ring will be relatively much larger than that in a proton ring of the same energy. Another reason of a high $V_{\rm rf}$ in an electron machine is to compensate for the energy loss due to synchrotron radiation. For example, in the high-energy ring of PEP II storing 9 GeV electrons, $V_{\rm rf} = 18.5$ MV is required. On the other hand, $V_{\rm rf}$ for the Fermilab Tevatron storing 1 TeV protons is only 2.16 MV. As a result, the synchrotron tunes for electron rings, $\nu_s \sim 0.01$, are usually an order of magnitude larger than those for proton rings, $\nu_s \sim 0.001$. For this reason, in the consideration of collective instabilities, the synchrotron period of the protons is sometimes much longer than the instability growth times. The wavelength of the perturbation or instability driving force is often of the same size as the radius or diameter of the vacuum chamber, which is usually much shorter than the length of a proton bunch. As a result, the proton bunches can be viewed locally as coasting beams in many instability considerations. Thus, each individual revolution harmonic can be considered as an independent mode. On the other hand, the electron bunch is mostly short, of the same size or even shorter than the diameter of the vacuum chamber. In other words, the electron bunch length can be of the same order or even shorter than the wavelength of the instability driving force. Therefore, for electron bunches, their bunch structure must be considered when studying their instabilities. Individual revolution harmonics are no longer independent and we need to study bunch modes instead.

6.1.1 Dispersion Relation

Let us first study the dispersion relation governing microwave instability of a proton beam [2]. Consider a coasting beam, with mean energy E_0 and mean velocity v_0. The unperturbed phase-space distribution is*

$$\psi_0(\Delta E) = \frac{N}{C_0} f_0(\Delta E) \ , \tag{6.4}$$

where $\psi_0(\Delta E)$ is normalized to the number of particle N in the beam when integrated over the energy offset ΔE and distance s along the closed orbit of the on-momentum orbit. The energy spread distribution $f_0(\Delta E)$ is normalized to unity when integrated over ΔE. Since the linear distribution of a coasting beam is uniform, ψ_0 does not depend on the location s or the time t. The length of the beam is therefore equal to the circumference C_0 of the accelerator ring. Note that here we are using t as the independent variable, because we are using a snap-shot description. The variables s and ΔE are used to describe the beam in the longitudinal phase space.

This stationary distribution is perturbed by an infinitesimal longitudinal density wave ψ_1 which is position dependent and evolves in time. At time t, we postulate the ansatz

$$\psi_1(s, \Delta E, t) = \hat{\psi}_1(\Delta E) e^{ins/R - i\Omega t} \ , \tag{6.5}$$

where $R = C_0/(2\pi)$ is mean radius of the closed orbit of an on-momentum particle, and $\Omega/(2\pi)$ the collective frequency of oscillation to be determined. Here, n denotes the revolution harmonic and $n = 0$ must be excluded, otherwise charge conservation will be violated. Actually, this is a snap-shot description; therefore the linear density will be periodic in s. By ansatz, we mean a postulation of the solution which must be verified to be consistent later. In fact, Eq. (6.5) can be considered as just one term of a Fourier series expansion. In other words, our postulation is the independence of each revolution harmonic or the revolution harmonics are good eigennumbers. When integrated over ΔE, we get the perturbation line density at time t,

$$\rho_1(s, t) = \hat{\rho}_1 e^{ins/R - i\Omega t} \ . \tag{6.6}$$

A test particle at the fixed location s monitors the perturbation wave passing through and experiences a wake force due to all beam particles that pass the location at an earlier

*The distribution in Eq. (6.4) can also be normalized to N by integration over ΔE and s/v_0 after the replacement of C_0 in the denominator by $T_0 = C_0/v_0$. In that case, dz should be replaced by dz/v_0 in Eq. (6.7), and v_0 should be deleted in Eqs. (6.8), (6.10), (6.11), and also the right side of Eqs. (6.8.

time. This force, averaged over the ring circumference, can be expressed as

$$\langle F_0^{\parallel}(s,t)\rangle = -\frac{e^2}{C}\int_0^{\infty} dz\,\rho_1(s,t-z/v_0)W_0'(z) = -\frac{e^2 v_0}{C_0}\,\rho_1(s,t)Z_0^{\parallel}(\Omega)\ , \tag{6.7}$$

where $Z_0^{\parallel}(\Omega)$ is the longitudinal impedance of the vacuum chamber evaluated at the collective frequency. There is a similar force acting on the particle from the wake of the unperturbed beam distribution by replacing ρ_1 with the unperturbed ρ_0 in Eq. (6.7). But that force has no time dependency and is of no interest to us here. In fact, this force will give a modified steady-state Hamiltonian and will contribute to the a modification of the unperturbed particle distribution, which we call potential-well distortion. Notice that the impedance samples the coherent frequency of the perturbation and has no knowledge of the revolution harmonic dependency. This is because the impedance is located at a fixed point along the ring. However, as we shall see below, the coherent frequency Ω does contain a harmonic content.

The particle energy will be perturbed according to the equation of motion Eq. (6.1)

$$\frac{d\Delta E}{dt} = -\frac{e^2 v_0}{T_0}Z_0^{\parallel}(\Omega)\hat{\rho}_1 e^{ins/R-i\Omega t}\ , \tag{6.8}$$

where $T_0 = C_0/v_0$ is the revolution period of the on-momentum particles.

Now let us pull out the Vlasov equation in its first order,

$$\frac{\partial\psi_1}{\partial t} + \frac{\partial\psi_1}{\partial s}\frac{ds}{dt} + \frac{\partial\psi_0}{\partial\Delta E}\frac{d\Delta E}{dt} = 0\ . \tag{6.9}$$

Substitution leads to

$$-i(\Omega - n\omega)\psi_1 = \frac{e^2 v_0 Z_0^{\parallel}(\Omega)}{T_0}\frac{d\psi_0}{d\Delta E}\,\hat{\rho}_1 e^{ins/R-i\Omega t}\ , \tag{6.10}$$

where $\omega = v/R$ and v are, respectively, the angular revolution frequency and velocity of a beam particle with energy offset ΔE. Next we have

$$\psi_1(s,\Delta E,t) = \frac{ie^2 v_0 Z_0^{\parallel}(\Omega)}{T_0}\frac{d\psi_0}{d\Delta E}\,\frac{\hat{\rho}_1 e^{ins/R-i\Omega t}}{\Omega - n\omega}\ . \tag{6.11}$$

Integrate both sides over ΔE. From Eq. (6.6), the left side is just the perturbation linear density which cancels $\hat{\rho}_1$ and the exponential on the right side, leaving behind

$$1 = \frac{ie^2 N Z_0^{\parallel}}{T_0^2}\int\frac{f_0'(\Delta E)}{\Omega - n\omega}\,d\Delta E\ , \tag{6.12}$$

where the unperturbed distribution f_0 in Eq. (6.4) that is normalized to unity has been used, and the prime is derivative with respect to ΔE. An integration by part leads to the dispersion relation

$$1 = \frac{ieI_0\eta n Z_0^{\parallel}(\Omega)\omega_0^2}{2\pi\beta^2 E_0}\int \frac{f_0(\Delta E)}{(\Omega - n\omega)^2}\, d\Delta E \ , \tag{6.13}$$

where use has been made to the relation

$$\frac{d\omega}{d\Delta E} = -\frac{\eta\omega_0}{\beta^2 E_0} \ , \tag{6.14}$$

and $I_0 = eN/T_0$ is the mean current of the beam. The negative sign on the right side of Eq. (6.14) comes about because the revolution frequency decreases as energy increases above transition. An immediate conclusion of Eq. (6.13) is that our ansatz for ψ_1 in Eq. (6.5) is correct and all revolution harmonics are decoupled[†]. Equation (6.13) is called a dispersion relation because it provides the relation of the collective frequency Ω to the wave number n/R. This collective frequency is to be solved from the dispersion relation for each revolution harmonic. If Ω has an imaginary part that is positive, the solution reveals a growth and there is a collective instability.

If there is no energy spread, the collective frequency can be solved easily. The collective frequency of oscillation is

$$\Omega = n\omega_0 + \omega_0\sqrt{\frac{eI_0\eta n^2}{2\pi\beta^2 E_0}}\ \sqrt{\frac{i\,\mathcal{R}e\, Z_0^{\parallel}(\Omega)}{n} - \frac{\mathcal{I}m\, Z_0^{\parallel}(\Omega)}{n}}\Bigg|_{\Omega\approx n\omega_0} \ , \tag{6.15}$$

of which the positive imaginary part is the growth rate. Writing it this way, the first square root is real above transition ($\eta > 0$), and there is no growth only when $Z_0^{\parallel}$ is purely inductive,

$$\frac{\mathcal{I}m\, Z_0^{\parallel}(n\omega_0)}{n} < 0 \ , \tag{6.16}$$

as postulated at the beginning of this chapter. By the same token, the beam is stable below transition if the impedance is purely capacitive. For a low-energy machine, the space charge impedance per harmonic is frequency independent and rolls off only at very high frequencies. Therefore above transition, the growth rate is directly proportional to

[†]This is true when only the linear terms are included in the Vlasov equation. For the inclusion of the lowest nonlinear terms, see Refs. [10, 11].

n or frequency. This is the source of *negative-mass instability* for a proton machine just above transition. The terminology comes about because the space charge force appears to be attractive above transition in binding particles together to form clumps as if the mass of the particles is negative. From Eq. (6.15), we can define

$$\omega_G = \omega_0 \sqrt{-\frac{\eta i e I_0 n Z_0^{\|}}{2pi\beta^2 E_0}} \tag{6.17}$$

as the growth rate without damping due to energy spread. Close examination reveals some similarity of this definition with the expression of synchrotron angular frequency ω_s. We can therefore interpret ω_G as the synchrotron angular frequency inside a bucket created by the interaction of the beam current I_0 with the longitudinal coupling impedance $Z_0^{\|}$ at the revolution harmonic n. The factor $-i$ takes care of the fact that the voltage created has to be 90° out of phase with the current so that a bucket can be formed.

Now let us consider a realistic beam that has an energy spread. Since ω is a function of the energy offset ΔE, define a revolution frequency distribution $g_0(\omega)$ for the unperturbed beam such that

$$g_0(\omega)d\omega = f_0(\Delta E)d\Delta E \ . \tag{6.18}$$

Substituting into Eq. (6.13) and integrating by part, we obtain

$$1 = -\frac{ieI_0\eta Z_0^{\|}(\Omega)\omega_0^2}{2\pi\beta^2 E_0} \int \frac{g_0'(\omega)}{\Omega - n\omega}\, d\omega \ . \tag{6.19}$$

Given the frequency distribution $g_0(\omega)$ of the unperturbed beam and the impedance $Z_0^{\|}$ of the ring at roughly $n\omega_0$, the collective frequency Ω can be solved from the dispersion equation. For a given revolution harmonic n, there can be many solutions for Ω. However, we are only interested in those that have positive imaginary parts. This is because if there is one such unstable solution, the system will be unstable independent of how many stable solutions there are. However, there is a subtlety in dealing with solution on the edge of stability, that is, when Ω is real. The dispersion relation will blow up when $n\omega = \Omega$ during the integration. This subtlety can be resolved if the problem is formulated as an initial value problem, which we will discuss in Chapter 14 on Landau damping. It will be shown that the proper way to go around the subtlety is to make the replacement

$$\frac{\Omega}{n} \longrightarrow \frac{\Omega}{n} + i\epsilon \ , \tag{6.20}$$

where ϵ is an infinitesimal positive real number and the harmonic n is considered positive. In other words, the path of integration in the ω-plane always goes under the Ω/n pole as illustrated in Fig. 6.2.

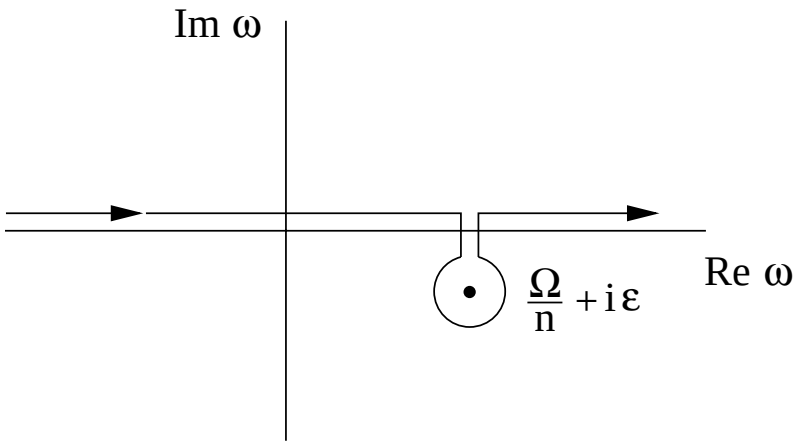

Figure 6.2: The path of integration in the dispersion relation must go below the Ω pole.

6.1.2 Stability Curve

For a Gaussian distribution, the integral in the dispersion relation is related to the complex error function, so that an analytic solution can be written down. For other distributions, one has to resort to numerical method. For a given growth rate or $\mathcal{I}m\,\Omega$, we perform the integral for various values of $\mathcal{R}e\,\Omega$ and read off $\mathcal{R}e\,Z_0^{\parallel}$ and $\mathcal{I}m\,Z_0^{\parallel}$ from the dispersion equation. Thus, we can plot a contour in the $\mathcal{R}e\,Z_0^{\parallel}$-$\mathcal{I}m\,Z_0^{\parallel}$ plane corresponding to a certain growth rate. This plot for the Gaussian distribution below transition is shown in Fig. 6.3. What are plotted is the real part U' and imaginary part V' of

$$U' + iV' = \frac{eI_0\beta^2(Z_0^{\parallel}/n)}{|\eta|E_0(\Delta E/E)^2_{\rm FWHM}} \tag{6.21}$$

at fixed growth rates. From outside to inside, the contours in the figure correspond to growth rates 0.5 to -0.5 in steps of -0.1 in units of HWHM of the frequency spread, where negative values imply damping. The contour corresponding to the stability threshold is drawn in dot-dashes and the area inside it is stable. Note that the positive V'-axis

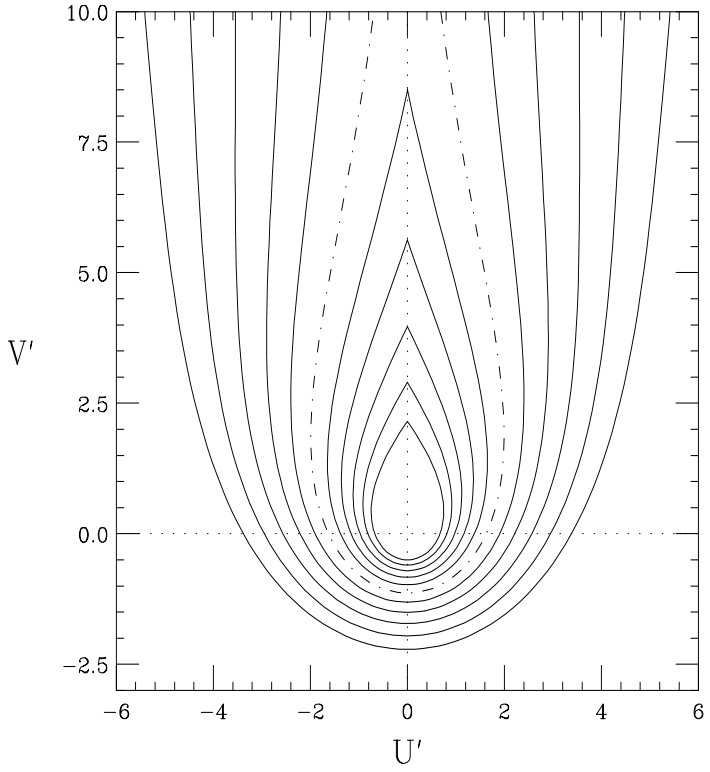

Figure 6.3: The growth contours for a Gaussian distribution in revolution frequency below transition. The abscissa U' and ordinate V' are, respectively, real and imaginary parts of $eI_0\beta^2(Z_0^{\parallel}/n)/[|\eta|E_0(\Delta E/E)^2_{\rm FWHM}]$. From outside to inside, the contours correspond to growth rates 0.5 to -0.5 in steps of -0.1 in units of HWHM of the frequency spread, where negative values imply damping. The contour corresponding to the stability threshold is drawn in dot-dashes and the area inside it is stable.

is a cut and those damping contours continue into other Riemann sheets after passing through the cut. Therefore, for each (U', V') outside the stability region bounded by the dot-dashed curve, there can also be one or more stable solutions. However, since there is at least one unstable solution, this outside region is termed unstable.

Obviously, these contours depend on the distribution $g_0(\omega)$ assumed. In Fig. 6.4, we plot the stability contours for various frequency distributions below transition. They are for frequency distributions, from inside to outside, $f(x) = \frac{3}{4}(1-x^2)$, $\frac{8}{3\pi}(1-x^2)^{3/2}$, $\frac{15}{16}(1-x^2)^2$, $\frac{315}{32}(1-x^2)^4$, and $\frac{1}{\sqrt{2\pi}}e^{-x^2/2}$. The innermost one is the parabolic distribution with discontinuous density slopes at the edges and we see that the stability contour

curves towards the origin in the positive V' region. The contour next to it corresponds

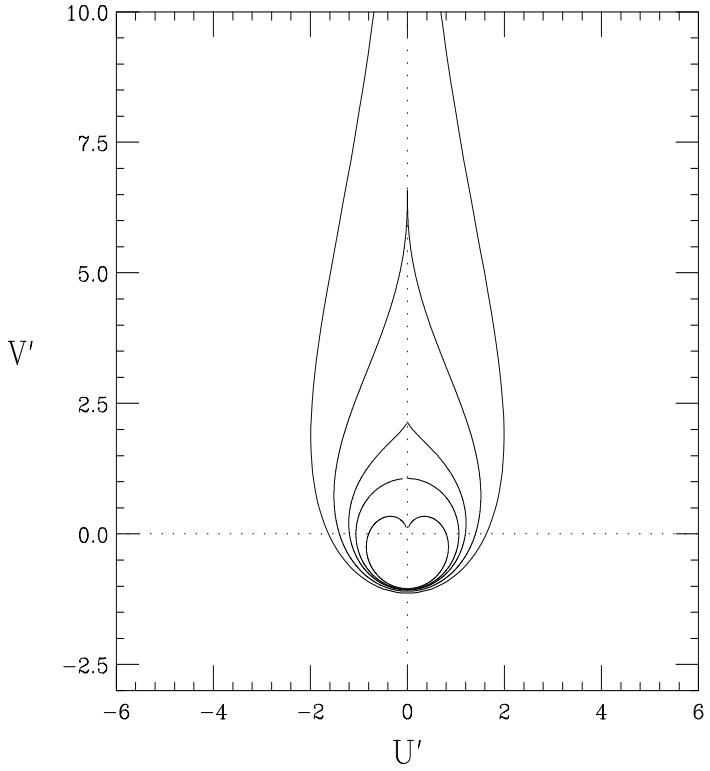

Figure 6.4: The stability contours for different frequency distribution below transition. The abscissa U' and ordinate V' are, respectively, real and imaginary parts of $eI_0\beta^2(Z_0^{\|}/n)/[|\eta|E_0(\Delta E/E)^2_{\rm FWHM}]$. From inside to outside, they correspond to unperturbed revolution frequency distribution $f(x) = \frac{3}{4}(1-x^2)$, $\frac{8}{3\pi}(1-x^2)^{3/2}$, $\frac{15}{16}(1-x^2)^2$, $\frac{315}{32}(1-x^2)^4$, and $\frac{1}{\sqrt{2\pi}}e^{-x^2/2}$. Note that all contours cut the V'-axis at about -1.

to continuous density slopes at the edges and it does not dip downward in the positive V' region. As the edges become smoother or with higher derivatives that are continuous, the contour shoots up higher in the upper half plane. For all distributions with a finite spread, the contours end with finite values at the positive V'-axis. For the Gaussian distribution which has infinite spread and continuous derivatives up to infinite orders, the contour will only approach the positive V'-axis without intersecting it.

We note in Fig. 6.4 that, regardless the form of distribution, all contours cut the negative V'-axis at ~ -1. Therefore, it is reasonable to approximate the stability region by a unit circle in the U'-V' plane, so that a stability criterion can be written analytically.

This is the *Keil-Schnell criterion* which reads [3] (Exercise 6.1)

$$\left|\frac{Z_0^{\|}}{n}\right| < F\frac{|\eta|E_0}{eI_0\beta^2}\left(\frac{\Delta E}{E_0}\right)^2_{\rm FWHM} , \tag{6.22}$$

where F is a distribution-dependent form factor and is equal to the negative V'-intersection of the contour. For all the distributions discussed here, $F \approx 1$. (See Exercise 6.1 below).

For a bunch beam, if the disturbance has a wavelength much less than the bunch length, we can view the bunch locally as a coasting beam. Boussard [4] suggested to apply the same Keil-Schnell stability criterion to a bunch beam by replacing the coasting beam current I_0 with the peak current $I_{\rm peak}$ of the bunch. Krinsky and Wang [6] performed a vigorous derivation of the microwave stability limit for a bunch beam with a Gaussian energy spread and found the stability criterion

$$\left|\frac{Z_0^{\|}}{n}\right| < \frac{2\pi|\eta|E_0}{eI_{\rm peak}\beta^2}\left(\frac{\Delta E}{E_0}\right)^2_{\rm rms} . \tag{6.23}$$

Comparing with Eq. (6.22), the Krinsky-Wang criterion corresponds to the Keil-Schnell criterion with a form factor of $\pi/(4\ln 2) = 1.133$, which is exactly the negative V'-intersect (see Exercise 6.1.) We want to point out that it is necessary for the Keil-Schnell criterion of Eq. (6.22) to be defined in terms of the *full width at half maximum* (FWHM) of the energy spread. Only such a reference will give a form factor that is close to unity for all reasonable distributions of the energy spread. This may be because the FWHM provides us with a more accurate measurement of the spread than the rms value. As an example, in terms of FWHM according to Eq. (6.22), the form factors for the Gaussian and the parabolic distributions are, respectively, and $F = \pi/(4\ln 2) = 1.133$ and $F = \pi/3 = 1.0472$. Since $\Delta E_{\rm FWHM} = 2\sqrt{2\ln 2}\Delta E_{\rm rms}$ for the Gaussian distribution and $\Delta E_{\rm FWHM} = \sqrt{10}\Delta E_{\rm rms}$ for parabolic distribution, if we express the stability criterion in terms of the rms energy spread as in Eq. (6.23), the form factors become $F = 1$ for the Gaussian distribution and $F = 5/3 = 1.67$ for parabolic the distribution.

6.1.3 Landau Damping

Keil-Schnell Criterion can be rearrange to read

$$n\omega_0\sqrt{\frac{e|\eta||Z_0^{\|}/n|I_0}{2\pi\beta^2E_0}} < n\omega_0\sqrt{\frac{F}{2\pi}}\frac{|\eta|\Delta E|_{\rm FWHM}}{\beta^2E_0} . \tag{6.24}$$

The left side is the growth rate without damping as discussed in Eq. (6.17) with I_0 replaced by $I_{\rm peak}$ in the case of a bunch. The right side can therefore be considered as the Landau damping rate coming from energy spread or frequency spread. Stability is maintained if Landau damping is large enough. The theory of Landau damping is rather profound, for example, the exchange of energy between particles and waves, the mechanism of damping, the contour around the poles in Eq. (6.13), etc. These will be studied in detailed in Chapter 14. The readers are also referred to the papers by Landau and Jackson [1, 7], and also a very well-written chapter in Chao's book [2].

6.1.4 Self-Bunching

Neglecting the effect of the wake function, the Hamiltonian for particle motion can be written as

$$H = -\frac{\eta}{2v\beta^2 E_0}(\Delta E)^2 + \frac{eV_{\rm rf}}{2\pi v h}\cos(h\omega_0\tau) \ , \tag{6.25}$$

where the synchronous angle has been put to zero and the small-bunch approximation has been relaxed. It is easy to see that the height of the bucket is

$$\Delta E|_{\rm bucket} = \sqrt{\frac{eE_0V_{\rm rf}}{\pi h|\eta|}} \ . \tag{6.26}$$

Keil-Schnell criterion can now be rearranged to read

$$\sqrt{\frac{eE_0I_0|Z_0^{\|}|}{\pi n|\eta|}} < \sqrt{\frac{F}{\pi\beta^2}}\Delta E|_{\rm FWHM} \ . \tag{6.27}$$

Comparing with Eq. (6.26), the left side can be viewed as the height of a bucket created by an induced voltage $I_0|Z_0^{\|}|$ while the right side roughly the half full energy spread of the beam. This induced voltage will bunch the beam just as an rf voltage does. If the self-bunched bucket height is less than the half full energy spread of the beam, the bunching effect will not be visible and beam remains coasting. Otherwise, the beam breaks up into bunchlets of harmonic n, and we call it unstable. This mechanism is known as *self-bunching*.

In fact, self-bunching is not so simple. The image current of the beam is rich in frequency components. For the component at the resonant frequency of the impedance, the voltage induced, called *beam loading voltage*, is in phase with the image current

or, more correctly, in opposite direction of the beam. Such voltage will not create any rf-like bucket at all, and therefore cannot produce self-bunching. Remember that when the beam is in the storage mode inside an accelerator ring, the rf voltage is at 90° to the beam current and the bucket created will be of maximum size—the so-called *stationary bucket* with synchronous angle $\phi_s = 0$ when the operation is below transition. As the synchronous angle ϕ_s increases, the angle between the rf voltage and the beam, or the *detuning angle* $\psi = \frac{\pi}{2} - \phi_s$, defined in Eq. (6.30)below, decreases and so is the bucket area—the so-called *moving bucket*. When the rf voltage is in phase with the beam, the synchronous angle $\phi_s = \frac{\pi}{2}$ and the bucket area shrinks to zero. In order for the beam image current to develop spontaneous self-bunching, the fields developed must be of such a phase and amplitude as to develop a real bucket of sufficient area to contain the beam. Although a small beam loading angle or a large synchronous angle will result in a small bucket area, however, as the beam frequency moves away too far from the resonance frequency, the beam loading voltage induced by the resonance impedance decreases also because the resonant impedance rolls off when the detuning is large. Consequently, there is a frequency deviation between the beam Fourier component and the resonance frequency at which the developed bucket area passes through a maximum. Some may argue that it is not the bucket area but the bucket height that sets the instability threshold, and the bucket height also goes through a maximum in between $\phi_s = 0$ and $\frac{\pi}{2}$. It is this bucket height that should enter into Eq. (6.26) for the stability criterion.

The impedance of a resonance is

$$Z_0^{\parallel}(\omega) = \frac{R_s}{1 - iQ\left(\frac{\omega}{\omega_r} - \frac{\omega_r}{\omega}\right)} \ , \tag{6.28}$$

where R_s is the shunt impedance, Q the quality factor, and ω_r the angular resonant frequency. When the frequency ω of the image current is close to the resonant frequency, we can write

$$Z_0^{\parallel}(\omega) \approx R_s \cos\psi \, e^{-i\psi} \ , \tag{6.29}$$

with the detuning angle defined as

$$\tan\psi = 2Q \, \frac{\omega_r - \omega}{\omega_r} \ . \tag{6.30}$$

Therefore, the beam loading voltage induced by the image current of frequency component ω will be proportional to $\cos\psi$ and at an angle ψ from the image current. Since $\psi = \frac{\pi}{2} - \phi_s$ and both the bucket area and height are proportional to the square root of

the voltage, we have,

$$\begin{aligned} \text{inducedbucket area} &\propto \alpha(\Gamma)\sqrt{\Gamma}\ , \\ \text{inducedbucket height} &\propto \beta(\Gamma)\sqrt{\Gamma}\ , \end{aligned} \tag{6.31}$$

where $\Gamma = \sin\phi_s = \cos\psi$. The parameter $\alpha(\Gamma)$ is the ratio of the moving bucket area to the stationary bucket area (when $\Gamma = 0$), and the parameter $\beta(\Gamma)$ is the ratio of the moving bucket height to the stationary bucket height [8]. The induced bucket area and bucket height area plotted against Γ in Fig. 6.5. We see that the induced bucket area

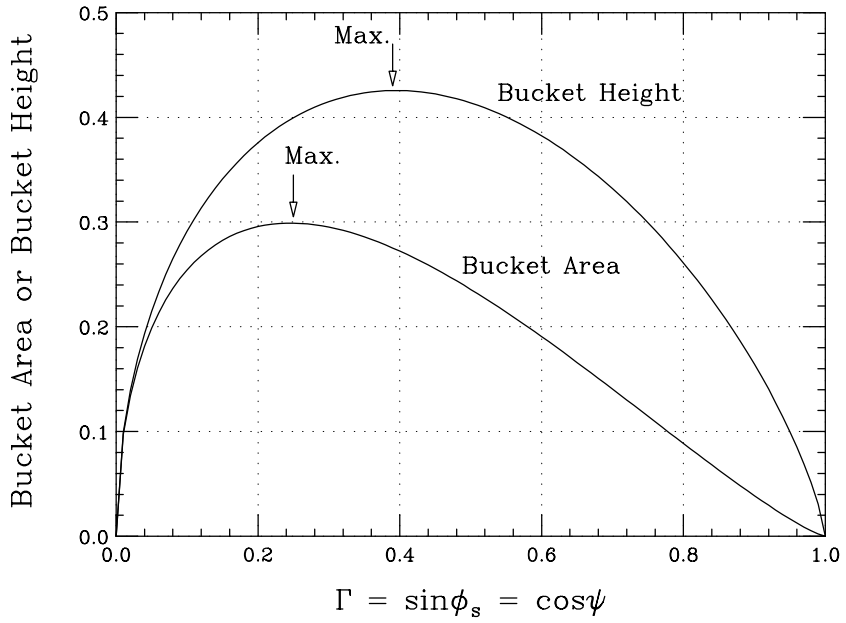

Figure 6.5: Plot showing the area and height of the bucket created by image current interacting with a resonant impedance. At a certain detuning ψ, describing the frequency offset of the image current Fourier component from the resonant frequency of the impedance, the induced bucket area or bucket height passes through a maximum. Self-bunching is most probable when the bucket area or bucket height is maximized.

has a maximum when $\Gamma = 0.25$ or the detuning angle $\psi = 76°$, while the induced bucket height has a maximum when $\Gamma = 0.39$ or the detuning angle $\psi = 67°$. From these results, the most probable frequency at which self-bunching takes place can be inferred.

There are two comments. First, our discussion above is for an accelerator operating below transition. The detuning angle is positive implying that the frequency shift is towards the inductive or low-frequency side of ω_r. When the accelerator is above

transition, the detuning will be towards the capacitive or high-frequency side of ω_r. This can be easily understood in a phasor-diagram description, which we will pursue in Chapter 7.5. The synchronous angle ϕ_s that we reference in this subsection is in fact the negative of the usual synchronous angle. This is because the beam loading voltage is essentially in the opposite direction of the beam current. Therefore the beam loading voltage will decelerate the beam instead of the usual acceleration by the rf voltage. However, the sign of ϕ_s does not affect the area or height of the induced bucket.

6.1.5 Overshoot

When the current is above the microwave threshold, the self-bunching concept tells us that there will be an increase in energy spread of the beam. The increase continues until it is large enough to stabilize the beam again according to the Keil-Schnell criterion. For a proton beam, experimental observation indicates that there will be an overshoot. Let $(\Delta E)_i$ be the initial energy spread which is below the threshold energy spread $(\Delta E)_{\rm th}$ postulated by the Keil-Schnell criterion. The final energy spread $(\Delta E)_f$ was found to be given empirically by [9]

$$(\Delta E)_i(\Delta E)_f = (\Delta E)_{\rm th}^2 \ . \tag{6.32}$$

Thus the final energy spread is always larger than the threshold energy spread. Overshoot formulas similar to but not exactly the same as Eq. (6.32) have been derived by Chin and Yokoya [10], and Bogacz and Ng [11]. For a bunch, the rf voltage introduces synchrotron oscillations. Thus, an increase in energy spread implies also eventual increase in bunch length. At the same time, the bunch area will be increased also.

The situation is quite different for electron bunches because of their short bunch lengths and the presence of radiation damping. This will be discussed in Chapter 7.

6.2 Observation and Cure

In order for a bunch to be microwave unstable, the growth rate has to be much faster than the synchrotron frequency. For the Fermilab Main Ring, the synchrotron period was typically about 100 to 200 turns or 2 to 4 ms. A naive way is to observe the microwave growth is to view the spectrum of the bunch over a large range of frequencies at a certain moment. However, the bunch spectrum produced by a network analyzer is usually via a

series of frequency filters of narrow width, starting from low frequencies and working its way towards high frequencies. This process is time consuming. As soon as the filtering reaches the frequencies concerned, typically a few GHz, the microwave growth may have been stabilized already through bunch dilution, and therefore no growth signals will be recorded. The correct way is to set the network analyzer at a narrow frequency span and look at the beam signal as a function of time. The frequency span is next set to an adjacent narrow frequency interval and the observation repeated until the frequency range of a few GHz has been covered. Besides, we must make sure that the network analyzer is capable of covering the high frequency of a few GHz for the microwave growth signals. The cable from the beam detector to the network analyzer must also be thick enough so that high-frequency attenuation is not a problem in signal propagation. Such an observation was made at the CERN Intersecting Storage Ring (ISR) which is a coasting beam machine. The network analyzer was set at zero span at 0.3 GHz. The beam current was at 55 mA. The signal observed from injection for 0.2 s is shown at the lower left corner of Fig. 6.6 in a linear scale. We see the signal rise sharply and decade very fast, implying an instability which saturates very soon. The beam current was next increased by steps to 190 mA and the observation repeated. We notice that with a higher beam current, the instability starts sooner and stays on longer. The center frequency of the network analyzer was next increased at the steps of 0.2 GHz and the observation repeated. The observation reveals an instability driven by a broadband impedance centering roughly at 1.2 GHz. Microwave instability can also be revealed in monitoring the longitudinal beam profiles, sometimes known as mountain ranges, via a wall resistance monitor. An example is shown in Fig. 6.8. From the ripples, the frequency of the driving impedance can be determined.

One way to produce microwave instability is to lower the rf voltage adiabatically. As the momentum spread of the bunch becomes lower than the Keil-Schnell criterion, microwave instability will develop. From the critical rf voltage, the momentum spread of the bunch can be computed and the impedance of the vacuum chamber driving the instability can be inferred. The rf voltage of the cavities in a proton synchrotron cannot be very much reduced, otherwise multi-pactoring will occur. The total voltage of the rf system can, however, be reduced by adjusting the phases between the cavities. For example, if the phase between two cavities is 180°, the voltages in these two cavities will be canceled. This is called paraphasing. For this reason, it is not possible to know the rf voltage exactly. Small errors in the paraphasing angles will bring about a large uncertainty in the tiny paraphased voltage. For this reason, the impedance determined

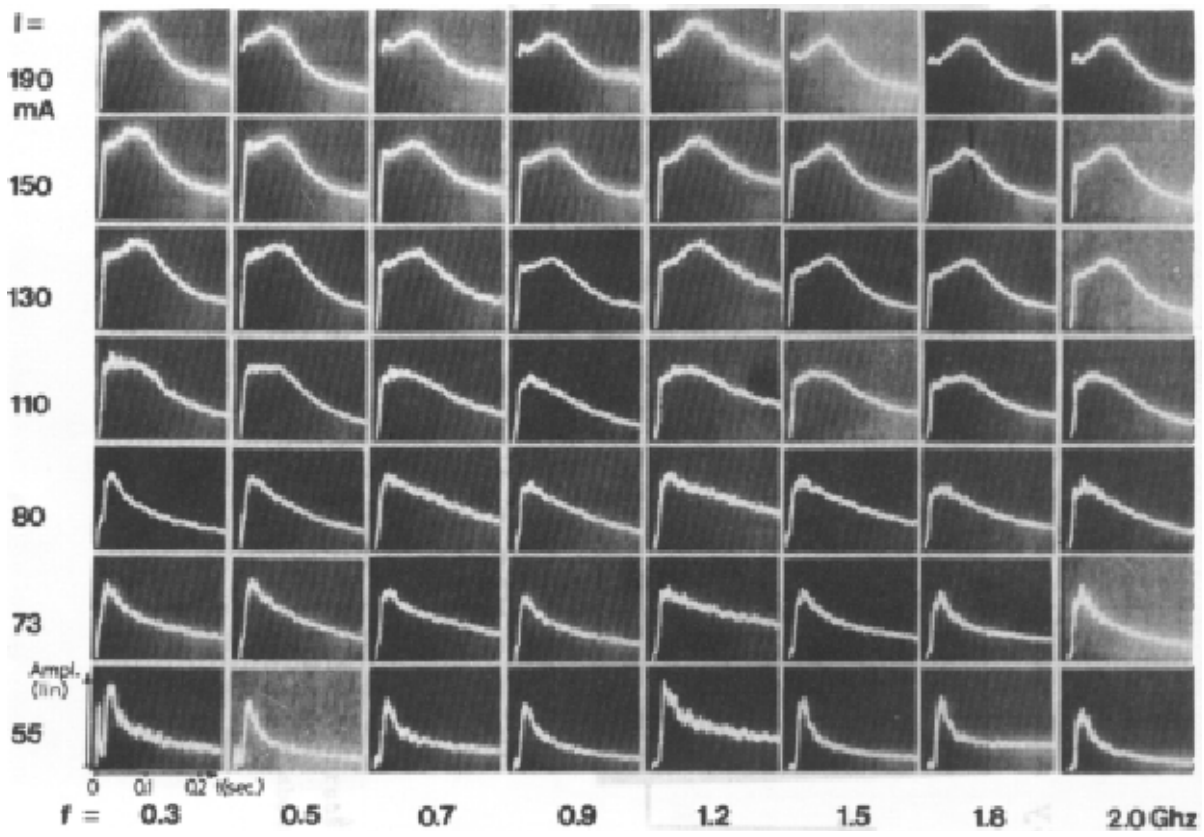

Figure 6.6: Pick-up signal after injection in the CERN ISR, for different observation frequencies but at zero span and different values of beam current. For high beam current, the signal grows before it decays.

by this method may not be accurate.

Another way to observe microwave instability is through debunching. The rf voltage is turned off abruptly and beam starts to debunch. During debunching, the local momentum spread decreases. When the latter is small enough, microwave instability occurs. From the time the instability starts, the impedance of the vacuum chamber can be inferred with the help of the Keil-Schnell criterion. In performing this experiment, the rf cavities must be shorted mechanically after the rf voltage is turned off. Otherwise, the beam will excite the cavities, a process called beam loading. The excited fields inside the cavities can bunch the beam developing high-frequency signals resembling signals of microwave instability. Such an experiment has been performed at the CERN Proton Synchrotron (CPS) and the observation is displayed in Fig. 6.7. The figure shows the time development at 2 ms per division. The top trace shows the rf

voltage which is turned off at 4 ms point. The network analyzer was set at a span from 1.5 to 1.8 GHz and the beam pick-up signal of the beam is shown in the lower trace. We see high-frequency beam signal start developing about 1 ms after the rf voltage is turned off. The signal grows for a few ms before it subsides. The shortcoming of this method of impedance measurement is the difficulty in determining the exact time when the microwave instability starts to develop. One must understand that the growth of the signal amplitude is exponential; therefore the very initial growth may not be visible.

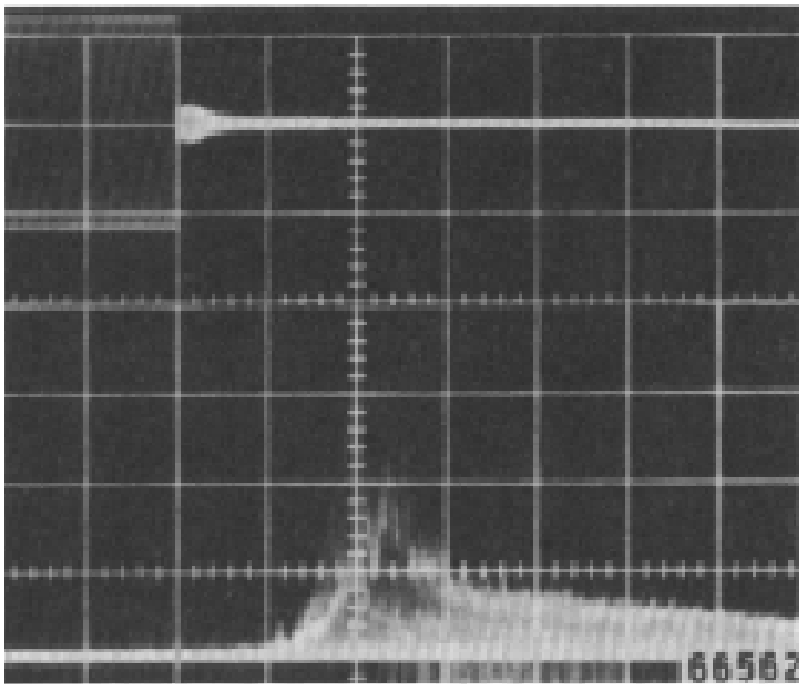

Figure 6.7: Microwave signal observed during debunching in the CERN CPS after the rf voltage (top trace) is turned off. The lower trace shows the beam signal at 1.5 to 1.8 GHz. The sweep is 2 ms per division.

Since microwave instability occurs so fast, it is not possible to use a damper system to cure it. One way to prevent the instability is to blow up the bunch so that the energy spread is large enough to provide the amount of Landau damping needed. Another way is to reduce the impedance budget of the ring by smoothing out the beam pipe discontinuities. For negative-mass instability driven by the space charge impedance just after transition, one can try to modify the ramp curve so that transition can be crossed faster. Of course, a γ_t-jump mechanism will be very helpful.

6.3 Ferrite Insertion and Instability

In Sec. 3.6, we discuss an experiment at the Los Alamos PSR where the space charge repulsive force is large compared with the available rf bunching force. Ferrite rings enclosed inside two pill-case cavities were installed into the vacuum chamber so that the beam would see an amount of inductive force from the ferrite, hoping that the space charge repelling force would be compensated. The experiment results show that this additional inductive force did cancel an appreciable amount of the space charge force of the intense proton beam to a certain extent. This is evident because the bunch lengths were shortened in the presence of the ferrite inserts with zero bias of the solenoidal current wound outside the ferrite tuners, and lengthened when the ferrite rings were biased. Also, the rf voltage required to keep the protons bunched to the required length had been lowered by about 1/3 in the presence of the ferrite insertion. At the same time the gap between successive proton beams was the cleanest ever seen, indicating that the rf buncher was able to keep the beam within the space charge distorted rf buckets so that no proton would leak out. However, the space charge compensation of the potential-well distortion had not been perfect. The ferrite insertion did lead to serious instability which we are going to discuss below.

6.3.1 Microwave Instability

The PSR was upgraded in 1998. The two previous ferrite tuners together with an additional one were installed in order to compensate for the space charge force of the higher intensity beam. However, an instability was observed [12]. With the rf buncher off, Fig. 6.8 shows the mountain-range plot of two consecutive turns of a chopped coasting beam accumulated for 125 μs and stored for 500 μs. The signals were recorded at a wide-band wall current monitor. The ripples at the beam profile indicate that a longitudinal microwave instability has occurred. The fast Fourier transform spectrum in Fig. 6.9 shows that the instability is driven at 72.7 MHz or the 26th revolution harmonic. The instability had also been observed in bunched beam. Ripples also show up at the rear half of a bunch, as recorded by a wall-gap monitor in Fig. 6.10. The top plots are two successive turns of a $\sim$ 250 ns (full width) bunch. Apparently, the instability is tolerable because ripples do not distort the shape of the bunch by too much. However, the $\sim$ 100 ns bunch on the lower plots is totally disastrous. The instability lengthens the bunch to almost 200 ns with very noticeable head-tail asymmetry.

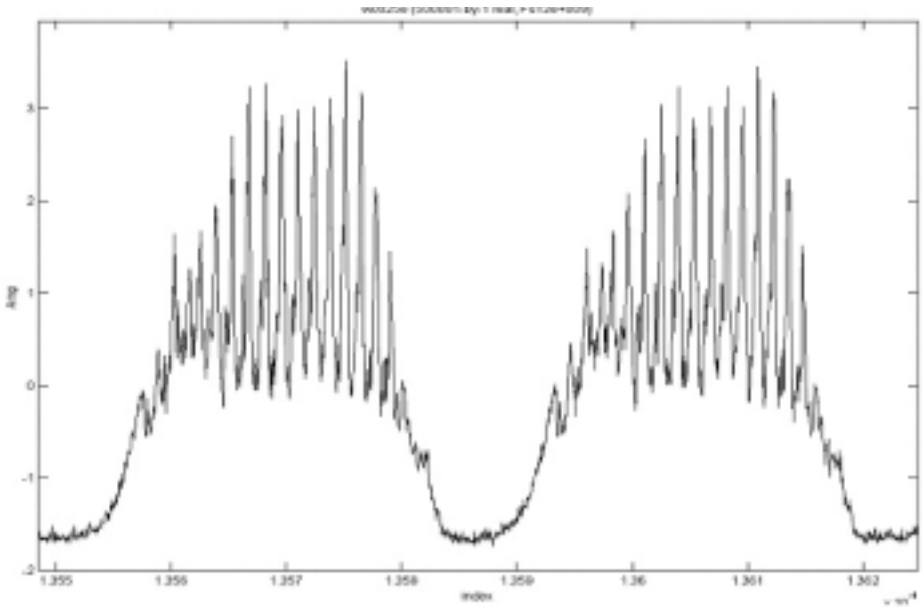

Figure 6.8: Beam profile of two consecutive turns of a chopped coasting beam recorded in a wall-gap monitor after storage of ~ 500 μs. The ripples show that a longitudinal microwave instability has occurred.

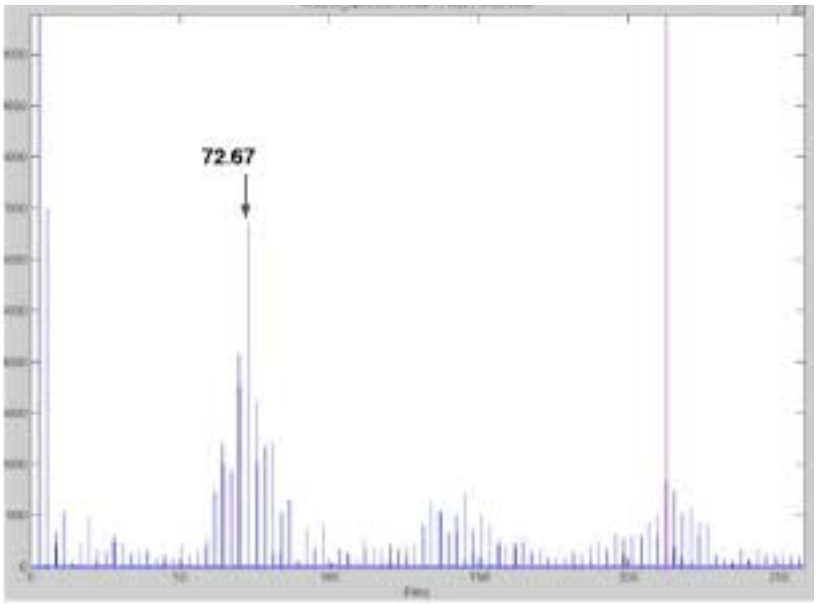

Figure 6.9: (color) Spectrum of the instability signal of the chopped beam in Fig. 6.8, showing the driving frequency is at 72.7 MHz.

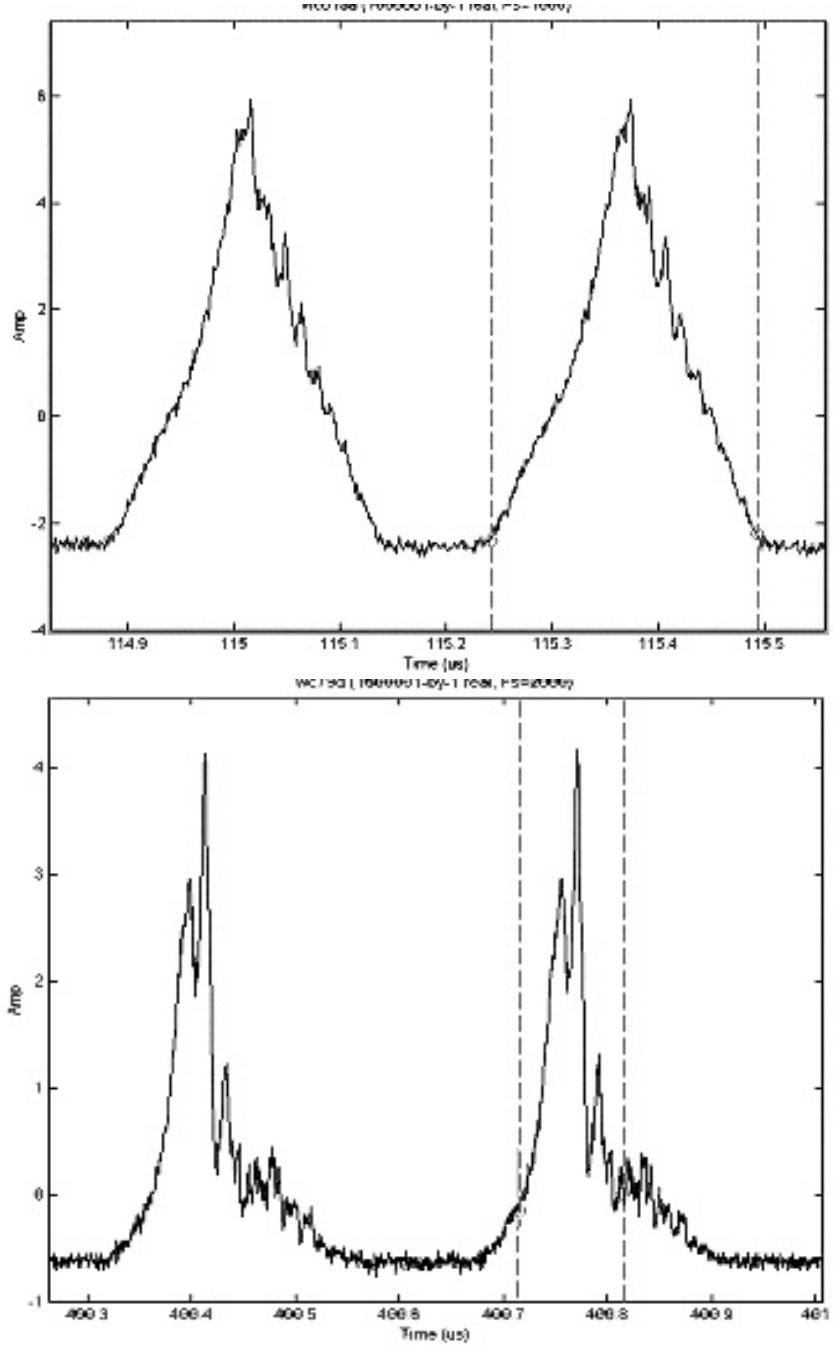

Figure 6.10: Instability perturbation on profiles of bunches with full width 250 ns (top) and 100 ns (bottom). The effect on the 250 ns bunch may be tolerable, but certainly not on the 100 ns bunch, which has lengthened almost to 200 ns.

6.3.2 Cause of Instability

In order to understand the reason behind the instability, let us first construct a simple model for the ferrite tuner. To incorporate loss, the relative permeability of the ferrite can be made complex[‡]: $\mu_s \to \mu_s' + i\mu_s''$. The impedance of a ferrite core of outer/inner diameter d_o/d_i and thickness t is therefore

$$Z_0^{\parallel} = -i(\mu_s' + i\mu_s'')\omega L_0 \ , \tag{6.33}$$

where $L_0 = \mu_0 t \ln(d_0/d_i)$ denotes the inductance of the ferrite if the relative permeability μ_s were unity. It is clear that μ_s' and μ_s'' must be frequency-dependent. Their general behaviors are shown in Fig. 6.11. For the Toshiba M_4C_{21A} ferrite, μ_s' is roughly constant at ~ 50 to 70 at low frequencies and starts to roll off around $\omega_r/(2\pi) \sim 50$ MHz, while μ_s'', being nearly zero at low frequencies, reaches a maximum near $\omega_r/(2\pi)$. The simplest

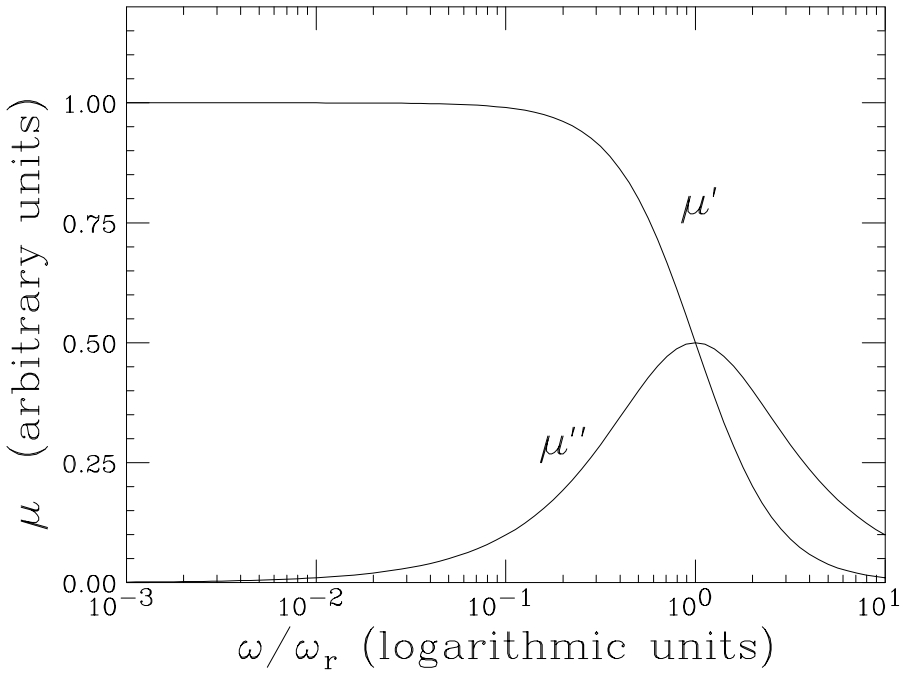

Figure 6.11: (color) Plot of μ' and μ'' as functions of frequency in the 2-parameter model. These are the typical properties of μ' and μ'' for most ferrites.

[‡]The subscript 's' signifies that the permeabilities are defined as if an inductor and a resistor are *in series*.

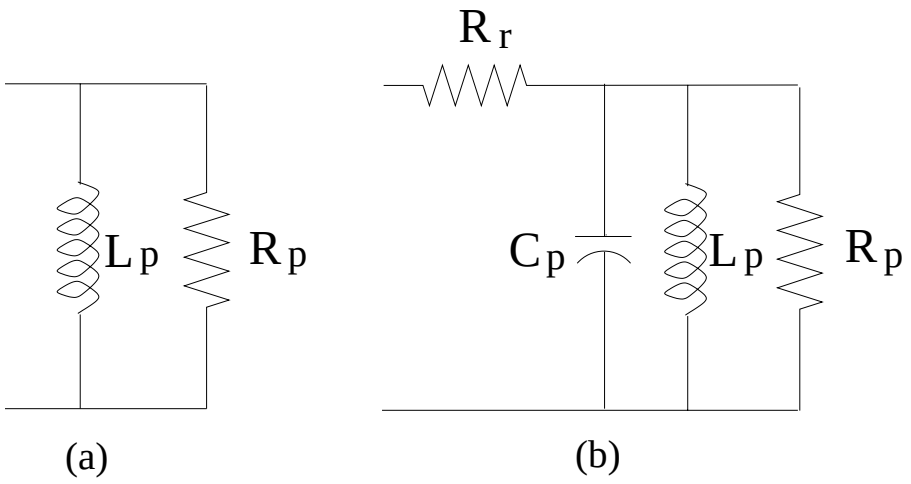

Figure 6.12: (a) Two-element model of ferrite. (b) Three-element model of ferrite cores enclosed in a pill-box cavity.

model for a piece of ferrite consists of an *ideal* inductance L_p and an *ideal* resistor R_p in parallel, as indicated in Fig. 6.12(a).

The impedance of the ferrite core is

$$Z_0^{\parallel}(\omega) = -i\omega L_p \frac{1 + i\omega/\omega_r}{1 + \omega^2/\omega_r^2} \ , \tag{6.34}$$

with a resonance at

$$\omega_r = \frac{R_p}{L_p} \ , \tag{6.35}$$

and

$$\mu_s' = \frac{L_p}{L_0} \frac{1}{1 + \omega^2/\omega_r^2} \ , \qquad \mu_s'' = \frac{L_p}{L_0} \frac{\omega/\omega_r}{1 + \omega^2/\omega_r^2} \ . \tag{6.36}$$

We see that the series μ_s' is relatively constant at low frequencies and starts to roll off when approaches ω_r, while μ_s'' increases as ω at low frequencies and resonates at ω_r. The corresponding longitudinal wake potential is

$$W(\tau) = R_p \left[\, \delta(\tau) - \omega_r e^{-\omega_r \tau} \, \right] . \tag{6.37}$$

When the ferrite is biased, L_p decreases so that μ_s' decreases. In this model, this is accomplished by a rise in the resonant frequency ω_r. Actually, measurements show that

the resonant frequency of μ_s'' does increase when the ferrite is biased. Thus, this simple 2-parameter model gives a very reasonable description of the ferrite.

With the ferrite cores enclosed in a pill-box cavity, a 3-parameter broadband parallel-RLC resonance model, as indicated in Fig. 6.12(b), appears to be more appropriate for the ferrite tuner as a whole. Sometimes there may be an additional residual resistance R_r which we neglect for the time being. We have, for the inductive insert,

$$Z_0^{\parallel}(\omega) = \frac{R_p}{1 - iQ\left(\dfrac{\omega}{\omega_r} - \dfrac{\omega_r}{\omega}\right)}, \tag{6.38}$$

where the resonant frequency is $\omega_r = (L_p C_p)^{-1/2}$ and the quality factor is $Q = R_p\sqrt{C_p/L_p}$.

For a space charge dominated beam, the actual area of beam stability in the complex $Z_0^{\parallel}/n$-plane (or the traditional U'-V' plane) is somewhat different from the commonly quoted Keil-Schnell estimation [3, 4]. In Fig. 6.13, the heart-shape solid curve, denoted by 1, is the threshold curve for parabolic distribution in momentum spread, where the momentum gradient is discontinuous at the ends of the spread. Instability develops and a smooth momentum gradient will result at the ends of the spread, changing the threshold curve to that of a distribution represented by 2, for example, $\frac{15}{16}(1 - \delta^2/\hat{\delta}^2)^2$, where δ is the fractional momentum spread and $\hat{\delta}$ the half momentum spread. Further smoothing of the momentum gradient at the ends of the spread to a Gaussian distribution will change the threshold curve to 3. On the other hand, the commonly known Keil-Schnell threshold is denoted by the circle of unit radius in dots. This is the reason why in many low-energy machines the Keil-Schnell limit has been significantly overcome by a factor of about 5 to 10 [5]. In this case, the space charge is almost the only source of the impedance, the real part of the impedance can be typically orders of magnitude smaller. As an example, if the impedance of the Los Alamos PSR is at Point A, the beam is within the microwave stable region if the momentum spread is Gaussian like, although it exceeds the Keil-Schnell limit. Now, if we compensate the space charge potential-well distortion by the ferrite inductance, the ferrite required will have an inductive impedance at low frequency equal to the negative value of the space charge impedance at A, for example, about -5.5 units according to Fig. 6.13. However, the ferrite also has a resistive impedance or $\mathcal{R}e\, Z_0^{\parallel}$ coming from μ_s''. Although $\mathcal{R}e\, Z_0^{\parallel}/n$ is negligible at low frequencies (for example, the rf frequency of 2.796 MHz of the PSR), it reaches a peak value near $\omega_r/(2\pi)$ (about 50 to 80 MHz for the Toshiba M_4C_{21A} inside the pill-box container) with the peak value the same order of magnitude as the low-frequency $\mathcal{I}m\, Z_0^{\parallel}$. Actually,

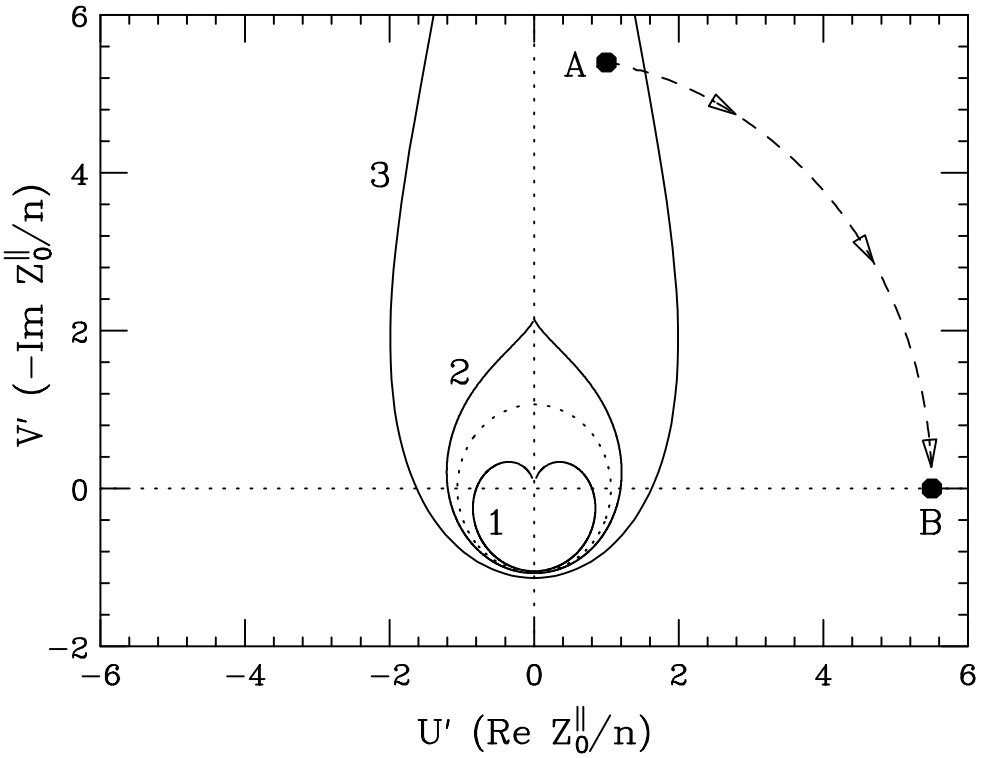

Figure 6.13: Microwave instability threshold curves in the complex $Z_0^{\|}$ (or U'-V') plane, for (1) parabolic momentum distribution, (2) distribution with a continuous momentum gradient, and (3) Gaussian momentum distribution. The commonly quoted Keil-Schnell threshold criterion is denoted by the circle in dots. An intense space charge beam may have impedance at Point A outside the Keil-Schnell circle and is stable. A ferrite tuner compensating the space charge completely will have a resistive impedance roughly at Point B and is therefore unstable.

according to the RLC model discussed above, we get approximately

$$\frac{\mathcal{R}e\, Z_0^{\|}/n|_{\rm pk}}{\mathcal{I}m\, Z_0^{\|}/n|_{\omega\to 0}} \approx \frac{Q^2+Q+1}{Q+2} = \left\{ \begin{array}{ll} Q & \text{if } Q \gg 1 \\ 1 & \text{if } Q \sim 1 \\ \frac{1}{2} & \text{if } Q \ll 1 \end{array} \right\} \geq \frac{1}{2}\ . \tag{6.39}$$

The RL model gives the same impedance ratio of $\frac{1}{2}$ as the low-Q case of Eq.(6.39). Thus the ferrite will contribute a resistive impedance denoted roughly by Point B (~ 5.5 units) when $Q \sim 1$ or at least one half of it when $Q \ll 1$. This resistive impedance of the ferrite insert will certainly exceed the threshold curve and we believe that the longitudinal instability observed at the Los Alamos PSR is a result of this consideration. It follows

from here that such low-frequency compensation of an intense space charge induced potential-well distortion will result in the microwave instability at high frequencies, $\omega \simeq \omega_r$. The conclusion appears to be that strong space charge potential-well distortion can only be compensated by the ferrite inductance to some extent to ensure that the resistive part of the ferrite insertion is kept below the microwave instability threshold. However, Eq. (6.39) is only correct when the RLC circuit is composed of an *ideal* resistor, an *ideal* inductor, and an *ideal* capacitor. In reality, the ferrite cores are much more complicated. To represent the inductor insert, many of these elements are frequency dependent. Thus, if one chooses the right ferrite in the construction of the inductive insert, it is possible to have the ratio of $\mathcal{R}e\, Z_0^{\parallel}/n|_{\rm pk}$ to $\mathcal{I}m\, Z_0^{\parallel}/n|_{\omega\to 0}$ much less than $\frac{1}{2}$. Such a ferrite will be the best candidate for space charge compensation.

6.3.3 Heating the Ferrite

One way to avoid the longitudinal microwave instability driven by the compensating ferrite is to choose a ferrite having the properties of high μ_s' at low frequencies and low loss[§] at high frequencies. Their ratio should be at least or larger than ~ 10. Past experience indicates that when a piece of ferrite is heated up, μ_s' will increase and hopefully the loss at high frequencies will decrease, thus having exactly the same properties that we are looking for.

A measurement of the temperature dependency of the ferrite has been made on a ferrite insert similar to those manufactured for the PSR was used, but much shorter containing only several ferrite cores. A sinusoidal wave was introduced from one end of the ferrite tuner via an antenna while the transmitted wave was received with another antenna at the other end. What was measured was S_{21}, the forward transmission through the network (in this case cavity), or the attenuation of a passive network. The results are shown in Fig. 6.14 and reveal that the resonant loss peak drops by a factor of about 8 when the ferrite cores are heated from the room temperature of 23°C to 100°C.

A measurement of the permeability of the ferrite has also been made on a single Toshiba M_4C_{21A} ferrite core as a function of core temperature. To provide both a good electrical circuit path and a uniform core temperature, the core was encased in an aluminum test fixture before being placed on a hot plate. The top half of the test fixture

[§]Low loss does not imply low μ''. Whenever ferrite is used, for example in the inductor insert, there will be inevitably capacitance involved. Thus low loss actually implies low R_p.

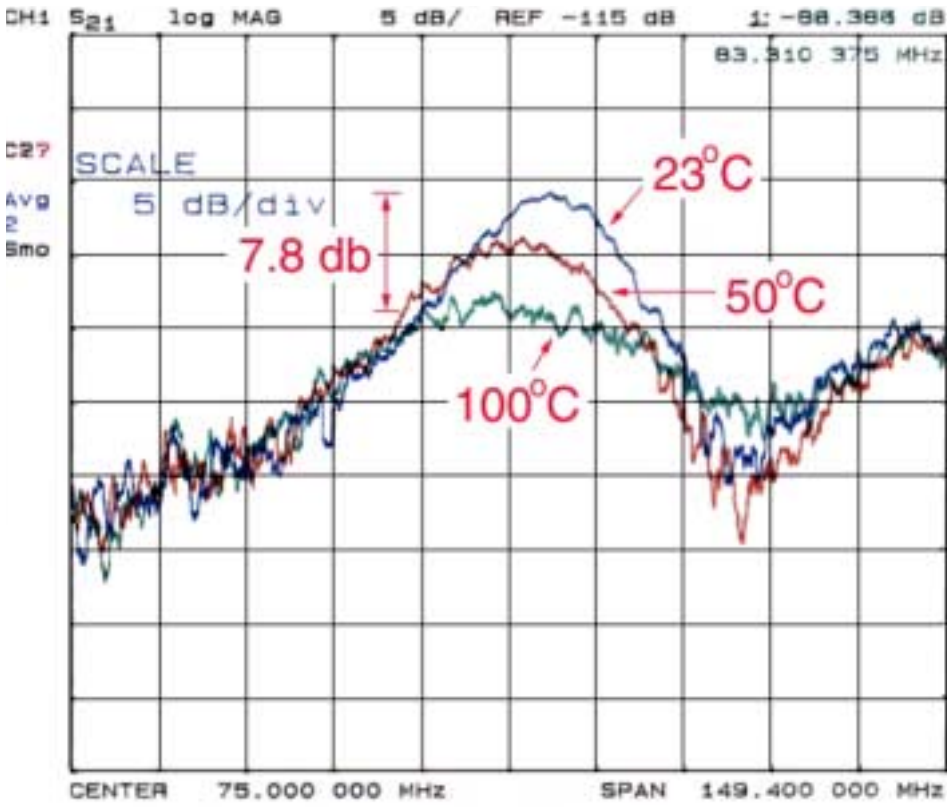

Figure 6.14: (color) An antenna at one end of the ferrite tuner sends out a sinusoidal wave to be picked up by another antenna at the other end of the tuner, and the loss is recorded. As the ferrite cores are heated from room temperature to 100°C, the loss has reduced by almost 8 times.

consisted of a machined aluminum disk, 9 in in diameter and 1.25 in thick. The inner section of the disk was machined out 0.005 in undersize to accommodate the ferrite core. The disk was then heated and the core was slipped into the disk. Upon cooling, the aluminum disk contracted and made a good thermal contact with one side and the outer edge of the ferrite core. The aluminum fixture and core were then flipped over onto a flat aluminum plate so that only the inner edge of the core was exposed. A good electrical connection between the aluminum disk and flat plate was made using strips of adhesive backed copper tape. The test fixture was placed on a hot plate and covered with two fire bricks. The test fixture was then heated to 175°C and allowed to cool slowly.

The impedance measurement was made by placing the probe of an HP4193A vector impedance meter directly across the inner edge of the ferrite core. Impedances were

measured from 10 MHz to 110 MHz in 10 MHz steps from 150°C to 25°C. The temperature of the core was monitored by a Fluke 80T-150U temperature probe inserted into a small hole in the aluminum disk portion of the test fixture.

In order to make an electrical model of the entire core and test fixture structure, it was necessary to obtain the equivalent parallel capacitance of the test set-up as depicted in Fig. 6.12(b). The capacitor C_p was determined by adding additional fixed 100 pf capacitors across the inner edge of the ferrite core and observing the change in the resonant frequency of the structure from 41 to 28 MHz, a frequency range in which the μ_s' of the ferrite is known to be relatively constant. In this manner, a capacitance of $C_p = 75$ pf was chosen to represent the equivalent parallel capacitance of the test circuit. There was also a series residual resistance of $R_r = 0.55\ \Omega$ in the probe. This residual resistance introduces a large error at low frequencies (below $\sim$ 10 Hz) when the resistive part of the RLC circuit is small. From the measurements of the input impedance, R_p and L_p were computed. From Eq. (6.36), the relative permeability, μ_s' and μ_s'' were inferred. These are plotted in Figs. 6.15 and 6.16. We see that from 23°C to 150°C, μ_s' at low frequencies has almost been doubled, implying that the inductance L_p at low frequencies has been doubled according to Eq. (6.36). The loss component μ_s'' also increases with temperature with its peak moves towards lower frequencies. This is obvious in the two-element model of a ferrite, because Eq. (6.36) says that the peak of μ_s'' is proportional to L_p and independent of R_p.

There is always a capacitance accompanied the ferrite insert. For a pill-box enclosing a single ferrite core, the capacitance measured was $C_p = 75$ pF, which is not too different from the computed value of 93 pF where a relative dielectric $\epsilon_r = 13$ has been assumed for the ferrite. The real part of the impedance of the ferrite insert per ferrite core, $\mathcal{R}e\, Z_0^{\|}$, is shown in Fig. 6.17. The resonant peaks are actually represented by the element R_p in the RLC circuit. The measured values of R_p as a function of frequency and temperature is shown in Fig. 6.18. We see that R_p depends very much on frequency and exhibits resonant peaks, which diminishes and moves to lower frequencies as the temperature increases. Thus the loss at high frequencies has been very much reduced by heating the ferrite. For a coasting beam, the energy lost to the ferrite core is given by the area under each $\mathcal{R}e\, Z_0^{\|}$ curve. Although both R_p and L_p vary tremendously with temperature, we find out that this loss is in fact temperature independent within 10% from 23°C to 150°C. However, the impedance becomes broader and broader and the resonant frequency shifts lower as the temperature increases.

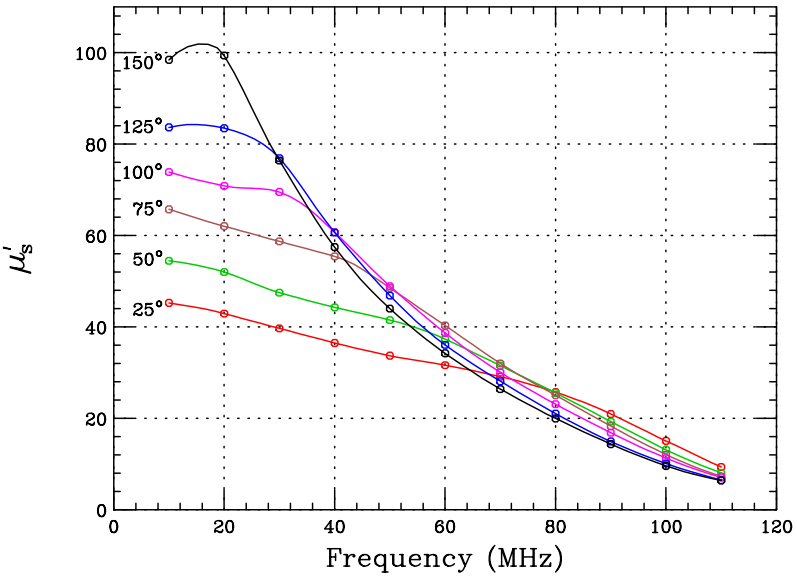

Figure 6.15: (color) Measured real part of the series magnetic permeability, μ_s' of a single Toshiba M_4C_{21A} ferrite core up to 110 MHz at 25°, 50, 75, 100, 125, and 150°C. Measured points are denoted by circles.

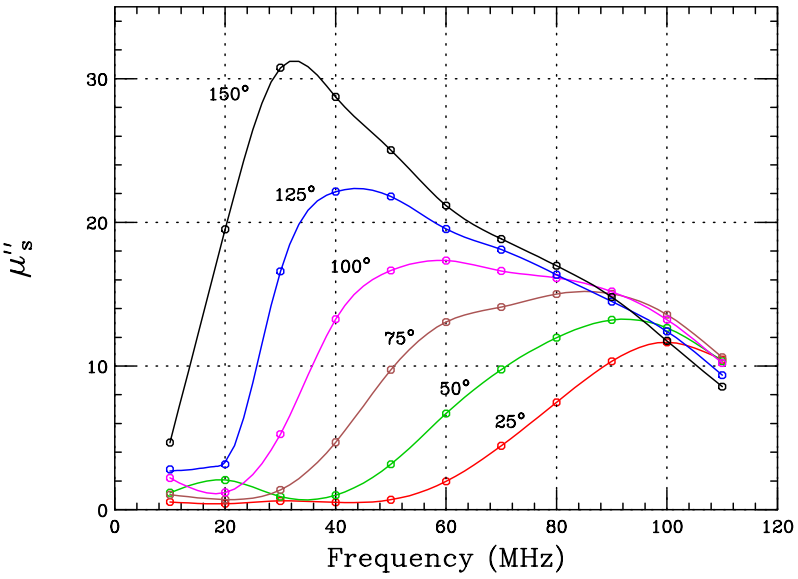

Figure 6.16: (color) Measured imaginary part of the series magnetic permeability, μ_s'' of a single Toshiba M_4C_{21A} ferrite core up to 110 MHz at 25°, 50, 75, 100, 125, and 150°C. Measured points are denoted by circles.

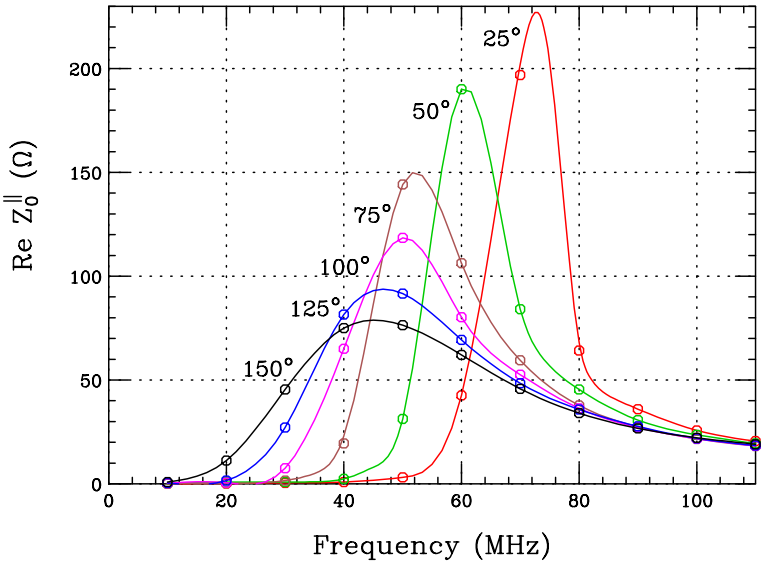

Figure 6.17: (color) Measured real part of the impedance of a single Toshiba M_4C_{21A} ferrite core inside an enclosing pill-box cavity up to 110 MHz at 25°, 50, 75, 100, 125, and 150°C. Measured points are denoted by circles.

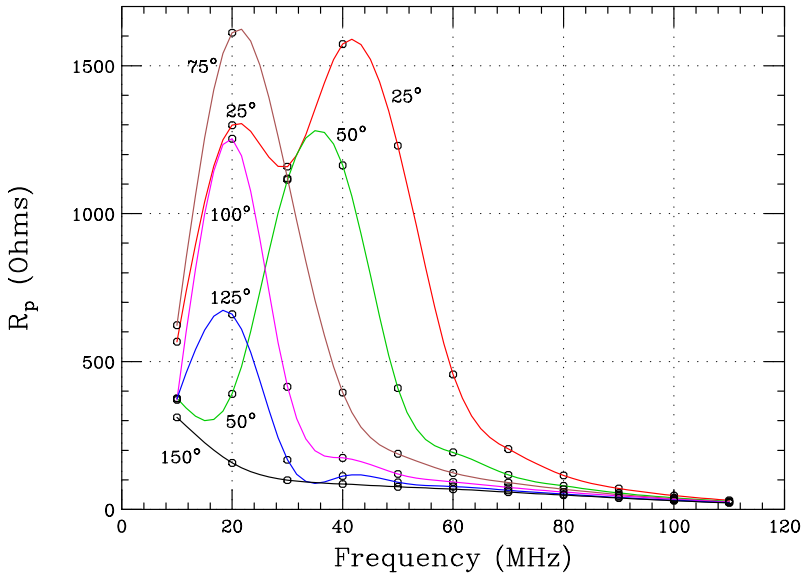

Figure 6.18: (color) Measured resistance of the resistor R_p in the RL model of the Toshiba M_4C_{21A} ferrite core or the RLC model of the inductor insert as functions of frequency at 25°, 50, 75, 100, 125, and 150°C. Measured points are denoted by circles.

The threshold microwave instability, depicted in Fig. 6.13, is determined by the impedance per unit PSR revolution harmonic, $Z_0^{\|}/n$, whose real and imaginary parts are shown, respectively, in Figs. 6.19 and 6.20. We now see that the resonant peak of $\mathcal{R}e\, Z_0^{\|}/n$ decreases with increasing temperature (except at 25°C). This explains why microwave instability can be alleviated by heating the ferrite cores.

The properties of the heated ferrite can be understand as follows. A piece of ferrite consists of domains with magnetization. The total magnetization is the vector sum of the magnetization of the domains. When the temperature increases, the domain magnetizations are freer to move. They tend to line up resulting in higher magnetic permeability μ_s', which is what we has been observing. However, if the temperature becomes too high, the spins of individual atoms or molecules become random and the total magnetization will drop and reach zero at the Curie temperature.

6.3.4 Application at the PSR

Later in 1999 the solenoids of the ferrite inserts for PSR were removed, the outside of the inserts were wound with heating tapes, and two modules were reinstalled in the PSR. When the ferrite is heated to 130°C, the longitudinal microwave instability, seen in the in Fig. 6.21, disappears. The profile of the 100 ns bunch in the presence of the heated ferrite tuners, is no longer distorted and the bunch has not been lengthened. Further beam studies with the heated ferrites carried out during the remainder of 1999 demonstrated other benefits of the inductors without unmanageable operational impacts.

Two effects of the ferrite inserts are thought to contribute to improving the instability threshold possibly in two ways. One is the effect of a cleaner gap that will trap fewer electrons during gap passage. This will improve the threshold of transverse e-p coupled-centroid instability (Chapter-19). The other is the increased momentum spread from the removal of the space charge depression of the bucket height. This will increase Landau damping and improve the threshold of longitudinal microwave instability. The latter increase in momentum spread is illustrated in Fig. 6.22 which shows plots from ACCSIM simulations [14]. The simulations show the effect of longitudinal space charge on the rf bucket height and momentum spread for a beam of 7.3 μC/pulse with 13 kV rf voltage. The left plot shows the bunch and the bucket without longitudinal space charge or the equivalent to full compensation by the inductive inserts. The right plot shows the bunch and bucket subject to the longitudinal space charge force. For this case, the

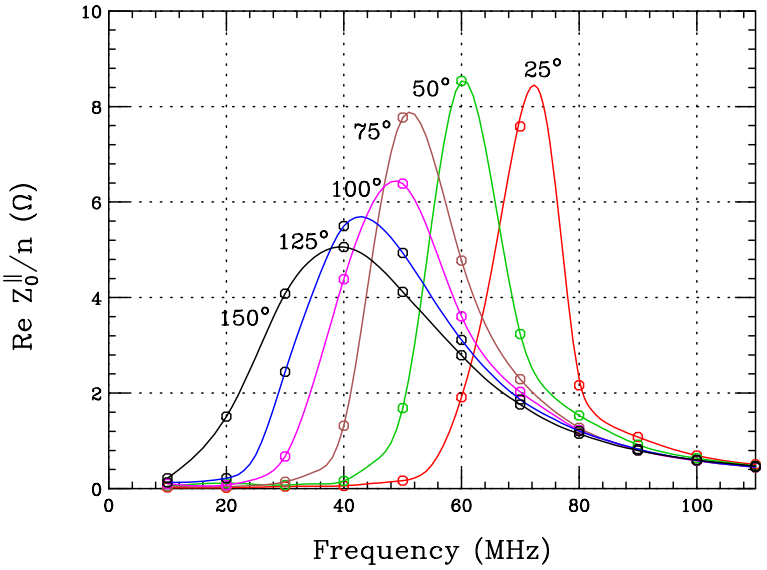

Figure 6.19: (color) Measured real part of the impedance per revolution harmonic of a single Toshiba M_4C_{21A} ferrite core inside an enclosing pill-box cavity up to 110 MHz at 25°, 50, 75, 100, 125, and 150°C. Measured points are denoted by circles.

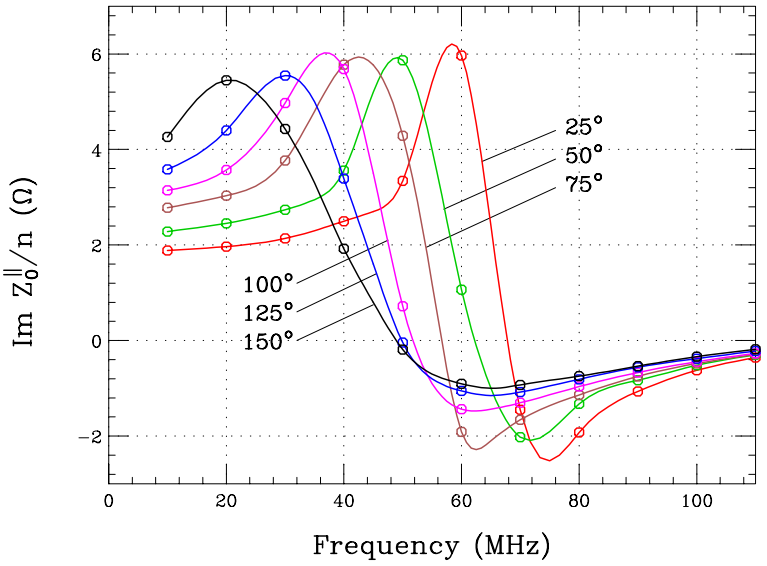

Figure 6.20: (color) Measured imaginary part of the impedance per revolution harmonic of a single Toshiba M_4C_{21A} ferrite core inside an enclosing pill-box cavity up to 110 MHz at 25°, 50, 75, 100, 125, and 150°C. Measured points are denoted by circles.

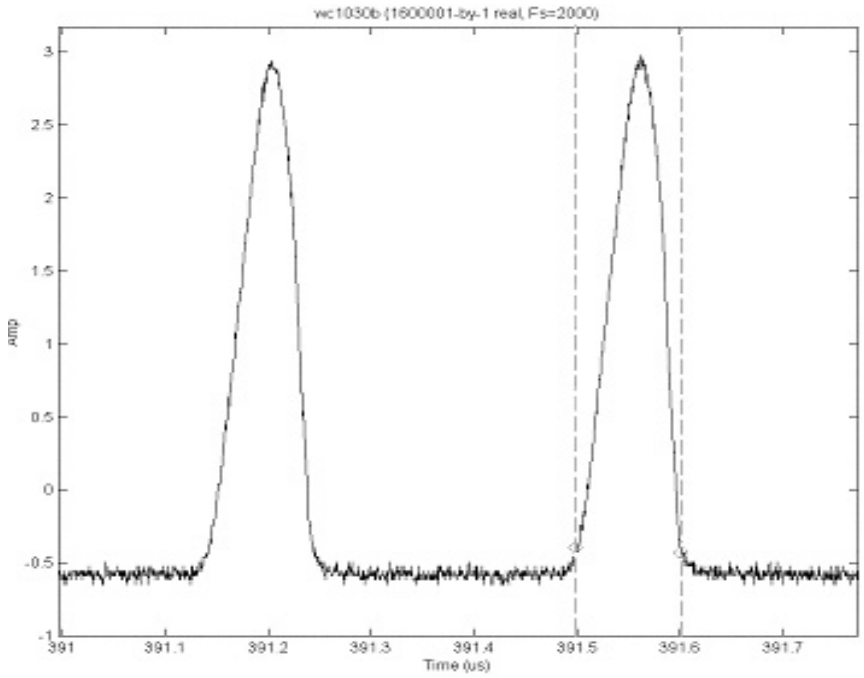

Figure 6.21: With two ferrite tuners installed and heated to 130°C, the instability ripples disappear from the profile of the 100 ns bunch.

space charge effect reduces the bucket height by $\sim$23%. In the absence of space charge, the bucket height scales by the square root of the rf voltage and would imply a reduction $\sim$41% in rf voltage to reach the same bucket height as with space charge. This argument implies that with inductors a $\sim$41% reduction in rf voltage would reach the same momentum spread as obtained in their absence. This is in reasonable agreement with the observed effect of $\sim$35%. Thus, it appears that Landau damping explains much of the effect of the ferrite inserts on the instability. With the increase in bucket height after the compensation of the space charge force by the inductive inserts, the bucket is able to hold the beam particles inside without leakage into the gap region. Thus, the ferrite inserts improve the thresholds of both the longitudinal microwave instability as well as the transverse two-stream coupled-centroid instability.

Comparable reductions in threshold curves have been obtained with other means of Landau damping such as the use of a skew quadrupole (coupled Landau damping), sextupoles and octupoles. It has also been observed that the effects of these (on the instability threshold) add with that of the inductors. An additional sextupole was installed in the upgrade. It is surprising that this sextupole has an important bearing

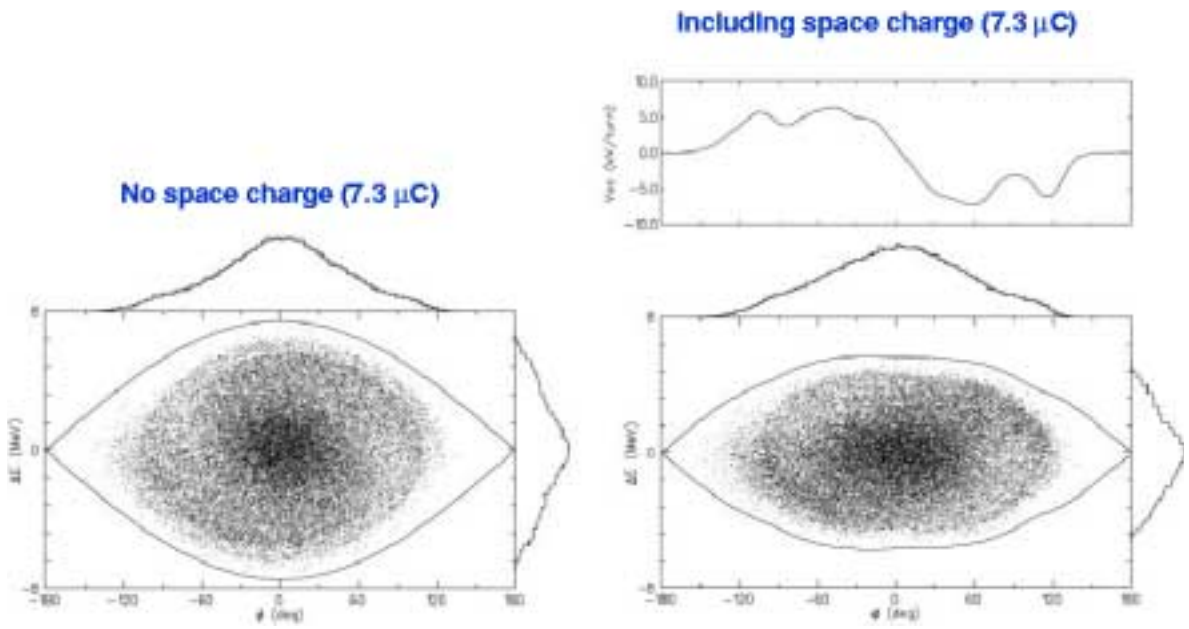

Figure 6.22: Simulation of a PSR bunch with an intensity of 7.3 μC at the buncher voltage of 13 kV using the code ACCSIM. The left plot is the result without space charge while the right plot is the result with space charge included. Notice that in the presence of space charge the bucket height is reduced by 24%, implying a cancellation of the rf voltage by 42%. The top curve on the right shows the space charge voltage per turn (proportional to the spatial derivative of the proton line density).

on the beam stability. Turning on this sextupole current to +20 A and optimizing the former four sextupoles and two octupoles in the ring can help to improve the threshold curve by $\sim$ 25% as is shown in Figure 6.23. It is understandable that the sextupoles and octupoles introduce tune spread which can provide Landau damping of the vertical coupled e-p instability once protons leak into the bunch gap and prevent the electrons from clearing. However, why just one sextupole has this much effect is not clear at all.

In late 1999 the combined effect of heated ferrites and a skew quad enabled us to accumulate and store at the PSR a record 9.7 μC/pulse, which is all that the linac could deliver. For this demonstration, the accumulation time was 1225 μs, the maximum obtainable at 1 Hz from the linac. The ferrite inserts were heated to 190°C, which over compensates longitudinal space charge by $\sim$50%. The rf buncher was at the maximum of 18 kV. In addition, the bunch width was stretched out to 305 ns, something never

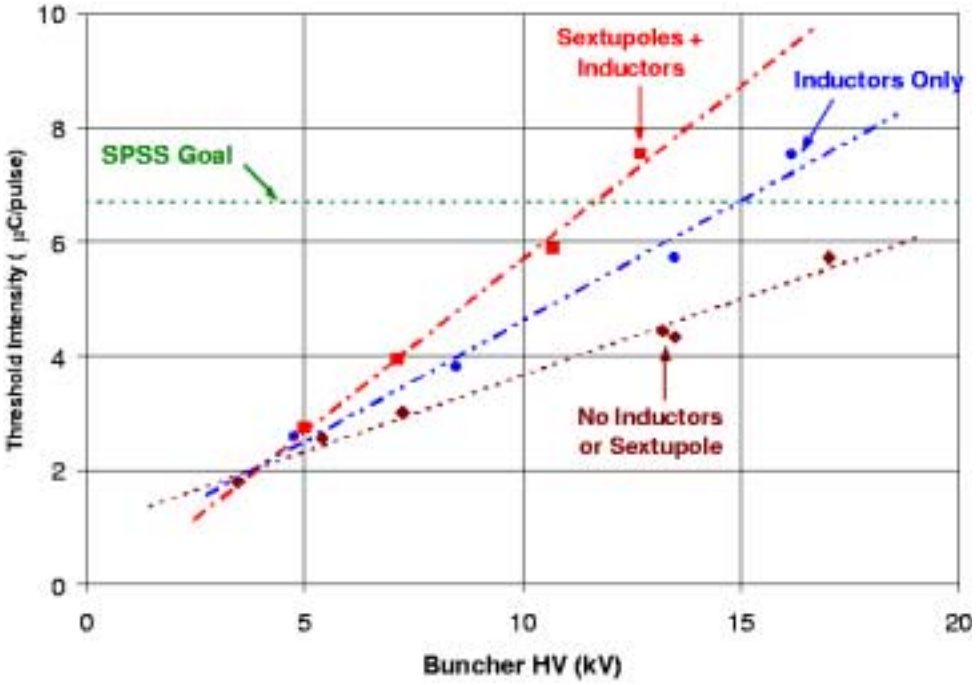

Figure 6.23: (color) After the upgrade, the PSR operating without the ferrite insert had a lower bunch intensity versus buncher voltage, depicted in dots, than the historical, depicted in dashes.

been accomplished before without reducing the threshold intensity. Beam losses were high ($\sim 5\%$), which would be prohibitive at 20 Hz. There was, no doubt, significant emittance growth that could be attributed to transverse space charge effects from the very high peak beam current of 82 A observed in this demonstration.

Engineered versions of the heated ferrites were installed in the fall of 2000 and have been used in production running ever since. A bunch length of 290 ns instead of the 250 has reduced the accumulation time accordingly thereby saving $\sim$\$15k per month in linac power costs. At the present, the PSR with two heated-ferrite modules can operate stably at an intensity of 8 μC/pulse for low repetition rates (for beam studies and single pulse users). Thus, the peak intensity goal of the upgrade has been surpassed. The remaining challenge is to reduce beam losses so that routine operation at 20 Hz is possible with acceptable activation of the ring.

6.4 Exercises

6.1. The dispersion relation of Eq. (6.19) can be rewritten in a simpler form. let us measure revolution angular frequency in terms of $2S$, the FWHM spread, which is related to the FWHM energy spread by

$$2S \equiv \omega - \omega_0\big|_{\rm FWHM} = -\frac{\eta\omega_0}{\beta^2}\,\frac{\Delta E}{E_0}\bigg|_{\rm FWHM} \ . \tag{6.40}$$

We can then introduce a dimensionless reduced angular frequency x such that

$$n\omega - n\omega_0 = nxS \qquad \text{and} \qquad \Omega - n\omega_0 = nx_1S \ , \tag{6.41}$$

where we have used the fact the the collective angular frequency Ω in Eq. (6.15) is close to $n\omega_0$. The frequency distribution function $g_0(\omega)$ is now transformed to a distribution $f(x)$ which is normalized to 1 when integrated over x. We have

$$\frac{dg_0(\omega)}{d\omega}d\omega = \frac{d\,f(x)}{dx}\frac{dx}{d\omega}dx = \frac{1}{S}\frac{d\,f(x)}{dx}dx \ . \tag{6.42}$$

(a) Show that the dispersion relation (6.19) becomes

$$1 = -\frac{i2\,\mathrm{sgn}(\eta)}{\pi}(U' + iV')\int\frac{f'(x)}{x_1 - x}dx \ , \tag{6.43}$$

where U' and V' are defined in Eq. (6.21).

(b) When the beam current is just above threshold, the reduced collective angular frequency is written as $x_1 = x_{1R} + i\epsilon$ where x_{1R} is real and ϵ is an infinitesimal positive number. Show that the stability curve can be obtained from

$$1 = -\frac{i2\,\mathrm{sgn}(\eta)}{\pi}(U' + iV')\left[\wp\int\frac{f'(x)}{x_{1R} - x}dx - i\pi f'(x_{1R})\right] \ . \tag{6.44}$$

by varying x_{1R}, where $\wp$ denotes the principal value of the integral.

(c) show that the negative V'-intersect or the lowest point of the bell-shaped stability curve $V'_{\rm in}$ is given by

$$1 = -\frac{2\,\mathrm{sgn}(\eta)V'_{\rm in}}{\pi}\,\wp\int\frac{f'(x)}{x}dx \ . \tag{6.45}$$

In fact, the form factor in the Keil-Schnell criterion is given by $F = |V'_{\rm in}|$.

(d) The form factor F's in the Keil Schnell criterion for various frequency distribution functions are listed in Table 6.1. Verify the results.

Table 6.1: Form factors in the Keil-Schnell criterion for various distributions. For the first four, the distributions reside only inside the region $|\Delta\omega| \le \widehat{\Delta\omega}$. When normalized to the HWHM, the domain becomes $|x| \le a$.

Frequency Distribution			**Form Factor**
$g_0(\omega) \qquad [\Delta\omega = \omega - \omega_0]$	$f(x)$		F
$\dfrac{3}{4\widehat{\Delta\omega}}\left(1-\dfrac{\Delta\omega^2}{\widehat{\Delta\omega}^2}\right)$	$\dfrac{3}{4a}\left(1-\dfrac{x^2}{a^2}\right)$	$a^2 = 2$	$\dfrac{\pi a^2}{6} = 1.0472$
$\dfrac{8}{3\pi\widehat{\Delta\omega}}\left(1-\dfrac{\Delta\omega^2}{\widehat{\Delta\omega}^2}\right)^{3/2}$	$\dfrac{8}{3\pi a}\left(1-\dfrac{x^2}{a^2}\right)^{3/2}$	$a^2 = \dfrac{1}{1-2^{-2/3}}$	$\dfrac{\pi a^2}{8} = 1.0612$
$\dfrac{15}{16\widehat{\Delta\omega}}\left(1-\dfrac{\Delta\omega^2}{\widehat{\Delta\omega}^2}\right)^{2}$	$\dfrac{15}{16a}\left(1-\dfrac{x^2}{a^2}\right)^{2}$	$a^2 = \dfrac{1}{1-2^{-1/2}}$	$\dfrac{\pi a^2}{10} = 1.0726$
$\dfrac{315}{256\widehat{\Delta\omega}}\left(1-\dfrac{\Delta\omega^2}{\widehat{\Delta\omega}^2}\right)^{4}$	$\dfrac{315}{256a}\left(1-\dfrac{x^2}{a^2}\right)^{4}$	$a^2 = \dfrac{1}{1-2^{-1/4}}$	$\dfrac{\pi a^2}{18} = 1.0970$
$\dfrac{1}{\sqrt{2\pi}\sigma}\exp\left(-\dfrac{\Delta\omega^2}{2\sigma^2}\right)$	$\dfrac{1}{\sqrt{2\pi}a}\exp\left(-\dfrac{x^2}{2a^2}\right)$	$a^2 = \dfrac{1}{2\ln 2}$	$\dfrac{\pi a^2}{2} = 1.1331$

6.2. Using Eq. (6.44), plot the bell-shaped stability contours for the distributions listed in Table 6.1 as illustrated in Fig. 6.4.

6.3. Using Eq. (6.43), show that the constant-growth contours for the Gaussian distribution are given by

$$1 = \frac{i\,\mathrm{sgn}(\eta) 4\ln 2}{\pi}(U' + iV')\left[1 + i\sqrt{\pi\ln 2}\; x_1\, w(\sqrt{\ln 2}\, x_1)\right] , \tag{6.46}$$

where use has been made of the integral representation of the complex error function:

$$w(z) = \frac{i}{\pi}\int_{-\infty}^{\infty}\frac{e^{-t^2}}{z-t}dt \qquad \text{for } \mathcal{I}m\, z > 0 \ . \tag{6.47}$$

Plot the contours in Fig. 6.3.

Bibliography

[1] L.D. Landau, J. Phys. USSR **10**, 25 (1946);

[2] A.W. Chao, *Physics of Collective Beam Instabilities in High Energy Accelerators*, John Wiley & Sons, 1993, p. 251.

[3] E. Keil and W. Schnell, CERN Report TH-RF/69-48 (1969); V.K. Neil and A.M. Sessler, Rev. Sci. Instr. **36**, 429 (1965).

[4] D. Boussard, CERN Report Lab II/RF/Int./75-2 (1975).

[5] J. Bosser, C. Carli, M. Chanel, N. Madsen, S. Maury, D. Möhl, G. Tranquille, Nucl. Instrum. and Meth. A**441**, 1 (2000).

[6] S. Krinsky and J.M. Wang, Particle Accelerators **17**, 109 (1985).

[7] J.D. Jackson, Plasma Phys. **C1**, 171 (1960).

[8] See for example, C. Bovet, et al., *A Selection of Formulae and Data Useful for the Design of A.G. Synchrotron*, CERN/MPS-SI/Int. DL/70/4, 23 April, 1970.

[9] R.A. Dory, Thesis, MURA Report 654, 1962.

[10] Y. Chin and K. Yokoya, Phys. Rev. **D28**, 2141 (1983).

[11] S.A. Bogacz and K.Y. Ng, Phys. Rev. **D36**, 1538 (1987).

[12] K.Y. Ng, J.E. Griffin, D. Wildman, M. Popovic, A. Browman, D. Fitzgerald, R. Macek, M. Plum, and T. Spickermann, *Recent Experience with Inductive Insert at PSR*, Proceedings of 2001 Particle Accelerator Conference, June 11-22, 2001, Chicago.

[13] M. Popovic, private communication.

[14] F.W. Jones, G.H. Mackenzie, and H. Schönauer, *Accsim — A program to Simulate the Accumulation of Intense Proton Beams*, Proceedings of the 14th International Conference on High Energy Accelerators, Particle Accelerators **31**, 199 (1990).